International Journal of Multiphase Flow 35 (2009) 227–246

Contents lists available at ScienceDirect

International Journal of Multiphase Flow

journal homepage: www.elsevier.com/locate/ijmulflow

A coupled level set and volume-of-fluid method for sharp interface simulation of plunging breaking waves

Zhaoyuan Wang, Jianming Yang, Bonguk Koo, Frederick Stern *

IIHR-Hydroscience & Engineering, University of Iowa, Iowa City, IA 52242-1585, USA

ARTICLE INFO

Article history:
Received 20 February 2008
Received in revised form 9 September 2008
Accepted 12 November 2008
Available online 6 December 2008

ABSTRACT

A coupled level set and volume-of-fluid (CLSVOF) method is implemented for the numerical simulations of interfacial flows in ship hydrodynamics. The interface is reconstructed via a piecewise linear interface construction scheme and is advected using a Lagrangian method with a second-order Runge–Kutta scheme for time integration. The level set function is re-distanced based on the reconstructed interface with an efficient re-distance algorithm. This level set re-distance algorithm significantly simplifies the complicated geometric procedure and is especially efficient for three-dimensional (3D) cases. The CLSVOF scheme is incorporated into CFDShip-Iowa version 6, a sharp interface Cartesian grid solver for two-phase incompressible flows with the interface represented by the level set method and the interface jump conditions handled using a ghost fluid methodology. The performance of the CLSVOF method is first evaluated through the numerical benchmark tests with prescribed velocity fields, which shows superior mass conservation property over the level set method. With combination of the flow solver, a gas bubble rising in a viscous liquid and a water drop impact onto a deep water pool are modeled. The computed results are compared with the available numerical and experimental results, and good agreement is obtained. Wave breaking of a steep Stokes wave is also modeled and the results are very close to the available numerical results. Finally, plunging wave breaking over a submerged bump is simulated. The overall wave breaking process and major events are identified from the wave profiles of the simulations, which are qualitatively validated by the complementary experimental data. The flow structures are also compared with the experimental data, and similar flow trends have been observed.

1. Introduction

One challenge of the numerical simulations of ship flows is the highly dynamic interface between air and water, which undergoes complicated topological changes and involves strong air/water interactions, such as breaking waves, formation of spray, turbulence, and entrainment of air around ships. The location of this rapidly moving surface is unknown and needed as part of the solution.

A number of numerical methods have been developed over the past few decades (Hirt and Nichols, 1981; Osher and Sethian, 1988; Unverdi and Tryggvason, 1992; Sussman et al., 1994) for the interface modeling, among which two Eulerian-based methods, the level set (LS) and volume-of-fluid (VOF) methods, have been extensively employed for interface capturing in ship hydrodynamics community (Carrica et al., 2007; Dommermuth et al., 2004; Klemt, 2005; Iafrati et al., 2001; Yang and Stern, 2007a,b). These two methods are well suited for flows with large flow distortions and geometrical changes. In the LS method, the interface is described by the LS function which is defined as a signed distance function. The normal and curvature can be easily and accurately calculated from the continuous and smooth distance function. As compared to the VOF method, the LS method is easy to implement, and the extension to three-dimensional (3D) coordinate is simple and straightforward. However, one serious drawback of the LS method is that mass conservation is often violated. Due to the poor mass conservation property of the LS method, wave breaking, formation of spray and entrainment of air cannot be accurately captured. For example, although sufficient grid resolution is provided, some initially formed droplets or air bubbles tend to shrink in size and eventually disappear during the computations. This problem is especially serious when a coarse grid is used as will be demonstrated in the simulations conducted using the LS based code. In the VOF method, the interface is captured by the VOF function which represents the volume fraction occupied by the liquid phase in each computational cell. The VOF function is not continuous across the interface. In order to advect the VOF function, the interface needs to be reconstructed using a geometric technique. The VOF method has excellent mass conservation properties but it lacks accuracy for the direct calculations of normal and curvature due to the discontinuous spatial derivatives of the VOF function near the interface. Moreover, the implementation of the VOF method is difficult since a complicated geometric procedure is needed for the interface reconstruction.

* Corresponding author. Tel.: +1 319 335 5215; fax: +1 319 335 5238.
E-mail address: frederick-stern@uiowa.edu (F. Stern).

0301-9322/$ - see front matter © 2008 Elsevier Ltd. All rights reserved.
doi:10.1016/j.ijmultiphaseflow.2008.11.004

Attempts have been made to improve the mass conservation property of the LS method by using higher order schemes (Peng et al., 1999), adaptive mesh refinement techniques to increase the local grid resolution (Strain, 1999; Sussman et al., 1999), and the hybrid particle level set (PLS) method (Enright et al., 2002). However, the inherent mass conservation problem still exists. A coupled level set and volume-of-fluid method (CLSVOF) has been explored (Bourlioux, 1995; Sussman and Puckett, 2000; Son and Hur, 2002; Son, 2003; Menard et al., 2007; Yang et al., 2007). The CLSVOF method takes advantage of both the LS and VOF methods where mass conservation is well preserved and the geometric properties, such as normal and curvature, can be easily estimated from the LS function. Another advantage of the combined method is that no major modifications are needed to the original LS based code. This will not only avoid additional coding work but also keep the desirable properties offered by the LS method, e.g., precise subcell location can be obtained from the LS function, which is necessary for the sharp interface treatment. However, the implementation of the CLSVOF method is not easy. This is because the VOF method alone is already difficult, the additional complexity to the CLSVOF method is the LS re-distance. In the CLSVOF method, the interface is usually reconstructed via a piecewise linear interface construction (PLIC) scheme and the LS function is re-distanced based on the reconstructed interface. The implementations of the CLSVOF method are different in the interface reconstruction, the advection of the VOF function and LS re-distance procedures. Bourlioux (1995) re-distanced the LS function based on the reconstructed interface in the cells that contain an interface. For cells without an interface, the LS function is re-distanced by solving the iteration equation (Sussman et al., 1994). In the study by Sussman and Puckett (2000), the LS function was assigned to be the exact distance from the reconstructed interface, where the interface was reconstructed using the least squares technique and advected via an Eulerian method. The similar scheme was used in the recent study by Menard et al. (2007), where modification was made in the least squares procedure in order to resolve very thin filaments. Son and Hur (2002) presented a geometrically based implementation scheme for two-dimensional (2D) and axisymmetric cases, which was later extended to the 3D case (Son, 2003). Yang et al. (2007) proposed an adaptive coupled level set and volume-of-fluid method for 2D problems on unstructured triangular grids.

In this study, the CLSVOF method is implemented in order to improve the mass conservation property for the numerical simulations of the interfacial flows in ship hydrodynamics. The VOF–PLIC scheme presented by Gueyffier et al. (1999) is employed for the interface reconstruction, which is based on a geometric description of the volume fraction truncated by the interface. The interface is advected using a Lagrangian method which has been found to be robust and efficient to implement, with relatively less complexity and difficulty to extend to three dimensions. In order to meet the requirement of a large range in spatial resolutions due to the complex flow structures of ship hydrodynamics, this method is extended to a non-uniform grid and the first-order time integration scheme is replaced by a second-order Runge–Kutta method. A LS re-distance algorithm is developed based on the PLIC scheme mentioned above. This algorithm significantly simplifies the complicated geometric procedure by finding the closest point on the reconstructed interface directly without considering the interface configuration in each computational cell. It is especially efficient for 3D cases where various possibilities of the interface configuration exist.

The CLSVOF scheme is incorporated into CFDShip-Iowa version 6, a sharp interface Cartesian grid solver for two-phase incompressible flows recently developed at IIHR (Yang and Stern, 2007a,b). In this solver, the interface is represented by the LS method. A ghost fluid methodology is adopted to handle the jump conditions across the interface, where the density and surface tension effect are treated in a sharp way while the viscosity is smeared by a smoothed Heaviside function. The primary objective herein is to develop the computational code with the capability for simulation details of wave breaking for ship hydrodynamics with present paper focusing on plunging wave breaking. The performance of the CLSVOF method is first evaluated through the numerical benchmark tests, such as slotted (Zalesak's) disk, Rider–Kothe single vortex flow, and 3D deformation field. In the benchmark tests, the velocity fields are prescribed without solving the flow equations. This allows the direct comparison of the interface modeling methods alone without the involvement of the flow solver. Verification and validation studies are conducted with combination of the flow equations, which include a gas bubble rising in a viscous liquid, water drop impact onto a deep water pool, and wave breaking of a steep Stokes wave. A gas bubble rising in a viscous liquid is simulated first in conjunction with the flow solver, where the bubble undergoes severe shape deformations. The simulation of a water drop impact onto a deep water pool is conducted, which involves complicated flow deformations such as coalescence, air entrainment, and jet bouncing. Wave breaking of a steep Stokes wave is modeled which serves as a verification test for the plunging wave breaking study. Finally, plunging wave breaking over a submerged bump is simulated to demonstrate the capability of the CLSVOF method to capture strong air/water interactions that commonly occur in ship hydrodynamics. The overall wave breaking process and major events are identified from the wave profiles of the simulations, which are qualitatively validated by the complementary experimental data. The flow structures are also compared with the experimental data, and similar flow trends have been observed.

2. Computational methods

2.1. Governing equations and interface jump conditions

For the incompressible viscous flows of two immiscible fluids with constant properties, the Navier–Stokes equations are given as follows

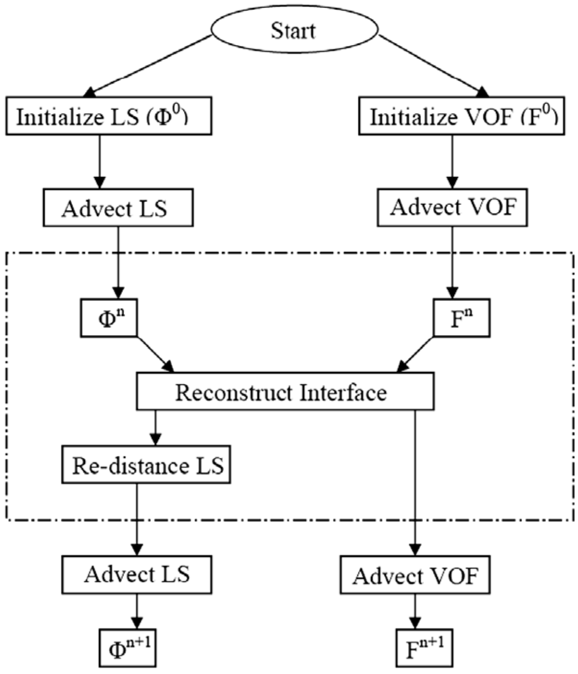

Fig. 1. Flow chart of the coupled level set and volume-of-fluid method.

$$\frac{\partial \mathbf{u}}{\partial t} + \mathbf{u}\cdot\nabla\mathbf{u} = \frac{1}{\rho}\nabla\cdot(-p\mathbf{I} + \mathbf{T}) + \mathbf{g}, \tag{1}$$

$$\nabla\cdot\mathbf{u} = 0, \tag{2}$$

where t is time, $\mathbf{u}$ is the velocity vector, p is pressure, $\mathbf{I}$ is the unit diagonal tensor, ρ is density, $\mathbf{g}$ represents the acceleration due to gravity, and $\mathbf{T}$ is the viscous stress tensor defined as

$$\mathbf{T} = 2\mu\mathbf{S}, \tag{3}$$

with μ the dynamic viscosity and $\mathbf{S}$ the strain rate

$$\mathbf{S} = \frac{1}{2}[\nabla\mathbf{u} + (\nabla\mathbf{u})^T], \tag{4}$$

where the superscript T represents transpose operation. Density and viscosity are discontinuous across the interface, which is a function of time and space. They will be defined using LS function later.

Since the fluids considered here are viscous and no phase change occurs, the velocity across the interface Γ is continuous:

$$[\mathbf{u}] = 0, \tag{5}$$

where [ ] denotes the jump at the interface, i.e., $f_L^I - f_G^I$ for a variable f with superscript I representing interface. The exact jump condition for stress is

$$[\mathbf{n}\cdot(-p\mathbf{I} + \mu(\nabla\mathbf{u} + (\nabla\mathbf{u})^T))\cdot\mathbf{n}] = \sigma\kappa, \tag{6}$$

where $\mathbf{n}$ is the unit vector normal to the interface, σ is the coefficient of surface tension, and κ is the local curvature of the interface. With a smoothed viscosity and continuous velocity field, the stress jump condition reduces to

$$[p] = p_L^I - p_G^I = -\sigma\kappa. \tag{7}$$

2.2. Interface representation and fluid properties

The interface is represented by the LS function which is corrected to enforce mass conservation with the aid of the VOF function. The LS function, ϕ, is defined as a distance function which is negative in the air, positive in the liquid, and zero at the interface. The VOF function, F, is defined as the liquid volume fraction in a cell with its value in between zero and one in a surface cell and zero and one in air and liquid, respectively.

The LS function and the VOF function are advanced using the following equations, respectively,

$$\frac{D\phi}{Dt} = \frac{\partial\phi}{\partial t} + (\mathbf{u}\cdot\nabla)\phi = 0, \tag{8}$$

$$\frac{DF}{Dt} = \frac{\partial F}{\partial t} + (\mathbf{u}\cdot\nabla)F = 0. \tag{9}$$

The LS advection equation is solved using the third-order TVD Runge–Kutta scheme (Shu and Osher, 1988) for time advancement and the fifth-order HJ-WENO scheme (Jiang and Peng, 1999) for spatial discretization. It should be noted that since the VOF function is not smoothly distributed at the free surface, an interface reconstruction procedure is required to evaluate the VOF flux across a surface cell. Finally, in order to achieve mass conservation, the LS functions have to be re-distanced prior to being used. This will be detailed in the next section.

Each phase of constant density and viscosity can be defined using the LS function in the computational domain and sharp jumps of the fluid properties occur at the phase interface. In this study, the density keeps its sharp jump and the viscosity is smoothed over a transition band across the interface,

$$\begin{aligned}\rho &= \rho_G + (\rho_L - \rho_G)H(\phi),\\ \mu &= \mu_G + (\mu_L - \mu_G)H_\varepsilon(\phi),\end{aligned} \tag{10}$$

where the subscripts G and L represent gas and liquid phase, respectively, the stepwise Heaviside function is

$$H(\phi) = \begin{cases} 1 & \text{if } \phi \geqslant 0 \\ 0 & \text{if } \phi < 0 \end{cases}, \tag{11}$$

and the smoothed Heaviside function is

$$H_\varepsilon(\phi) = \begin{cases} 1 & \text{if } \phi > \varepsilon \\ \frac{1}{2}\left[1 + \frac{\phi}{\varepsilon} + \frac{1}{\pi}\sin\left(\frac{\pi\phi}{\varepsilon}\right)\right] & \text{if } |\phi| \leqslant \varepsilon \\ 0 & \text{if } \phi < -\varepsilon \end{cases}, \tag{12}$$

where $\varepsilon = 1.5\Delta x$.

The geometric properties, i.e., the normal vector and curvature, can be estimated readily from the LS function,

$$\mathbf{n} = \frac{\nabla\phi}{|\nabla\phi|}, \tag{13}$$

$$\kappa = \nabla\cdot\left(\frac{\nabla\phi}{|\nabla\phi|}\right). \tag{14}$$

The flow equations are discretized on a staggered Cartesian grid with the convection terms approximated by a third-order QUICK scheme (Leonard, 1979) and other terms by the standard second-order central difference scheme. A semi-implicit time-advancement scheme

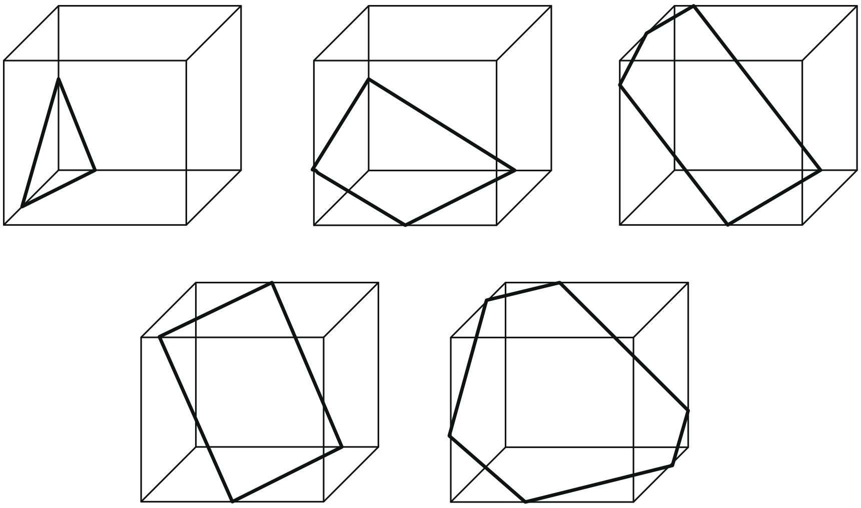

Fig. 2. Different configurations of the interface reconstruction.

is adopted to integrate the momentum equations with the second-order Crank–Nicolson scheme for the diagonal viscous terms and the second-order Adams–Bashforth scheme for the convective terms and other viscous terms. A four-step fractional-step method is employed for velocity–pressure coupling. The resulting pressure Poisson equation is solved using the PETSc library (Balay et al., 1997). The code is parallelized via a domain decomposition technique using the MPI library. Details of the numerical methods can be found in the studies by Yang and Stern (2007a,b).

3. CLSVOF method

In the CLSVOF method, the interface is reconstructed via a PLIC scheme from the VOF function and the interface normal vector which is computed from the LS function. Based on the reconstructed interface, the LS functions are re-distanced via a geometric procedure for achieving mass conservation. A flow chart for the CLSVOF algorithm is shown in Fig. 1. The coupling of the LS and VOF methods occurs during the interface reconstruction and the LS re-distance processes (shown in the dash-dotted box in Fig. 1).

3.1. Interface reconstruction

The interface reconstruction is to locate the interface by a specific scheme from the discrete VOF and LS functions, which serves two purposes: one is to calculate the VOF fluxes across the faces of each computational cell with an interface, and the other is to re-distance the LS function for achieving mass conservation. The VOF–PLIC scheme presented by Gueyffier et al. (1999) is employed for the interface reconstruction, where the interface is represented by a plane in a 3D computational cell,

$$\mathbf{n}\cdot\mathbf{x} = n_x x + n_y y + n_z z = \alpha, \tag{15}$$

where α is a parameter related to the shortest distance from the origin. Different numerical methods for the normal vector estimation can be found in Aulisa et al. (2007) in the context of the VOF method. In this study, the normal vector **n** can be easily obtained from the LS function. Once the normal vector **n** is known, the rest is to determine α from the *cut volume* defined by the VOF function. In the study by Gueyffier et al. (1999), the expression for the *cut volume* was derived with respect to α, normal vector **n** and grid spacing $\Delta\mathbf{x}$,

$$Volume = \frac{1}{6n_1n_2n_3}\left[\alpha^3 - \sum_{i=1}^{3} F_3(\alpha - n_i\Delta x_i) + \sum_{i=1}^{3} F_3(\alpha - \alpha_{\max} + n_i\Delta x_i)\right], \tag{16}$$

where $\alpha_{\max} = \sum_{i=1}^{3} n_i\Delta x_i$, n_i refers to n_x, n_y, n_z, and x_i denotes x, y, z with i = 1, 2, 3, respectively. $F_n(s)$ is defined as,

$$F_n(s) = \begin{cases} s^n & \text{for } s > 0 \\ 0 & \text{for } s \leqslant 0 \end{cases}.$$

For example, the term $F_3(\alpha - n_i\Delta x)$ in Eq. (16) can be written as:

$$F_3(\alpha - n_i\Delta x_i) = \begin{cases} (\alpha - n_i\Delta x_i)^3 & \text{if } \alpha - n_i\Delta x_i > 0 \\ 0 & \text{if } \alpha - n_i\Delta x_i \leqslant 0 \end{cases}.$$

Given the normal vector and grid spacing, the interface reconstruction is to find α by solving the "inverse" problem of Eq. (16) from a given *cut volume*. The "forward" problem is to find the *cut volume* from α through Eq. (16). Detailed analytical relations connecting the *cut volume* and α for both the "forward" and "inverse" problems are discussed by Scardovelli and Zaleski (2000). With a careful investigation of the geometry and the Eq. (16), the possible cases are reduced to five basic configurations as shown in Fig. 2. In order to meet the requirement of a large range in spatial resolutions due to the complex flow structures of ship hydrodynamics, a non-uniform grid is adopted in this study. Although the scheme and analysis (Gueyffier et al., 1999; Scardovelli and Zaleski, 2000) are based on a unitary cubic grid, its extension to a non-uniform grid is straightforward.

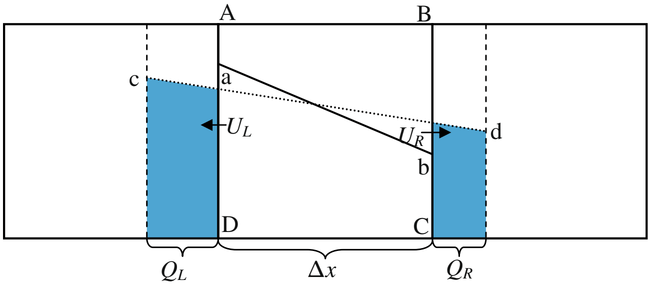

Fig. 3. Lagrangian interface propagation in two dimensions.

3.2. Lagrangian interface propagation

Once the interface is reconstructed, the VOF function in the whole computational domain can be updated. A Lagrangian interface propagation scheme is used in Gueyffier et al. (1999), which has been found to be robust and considerably simplifies programming with an operator splitting strategy to separately advance the interface in each spatial direction. The Lagrangian propagation scheme proposed by Gueyffier et al. (1999) is first-order accurate in time, in this study, a second-order Runge–Kutta scheme is used. The interface equation (15) at time t^n is written as,

$$n_x^{(n)}x^{(n)} + n_y^{(n)}y^{(n)} + n_z^{(n)}z^{(n)} = \alpha^{(n)}. \tag{17}$$

Since the interface advection in each spatial direction is similar, the following description is only given along x direction. As shown in Fig. 3, the x component of the velocity within cell *ABCD* is linearly interpolated

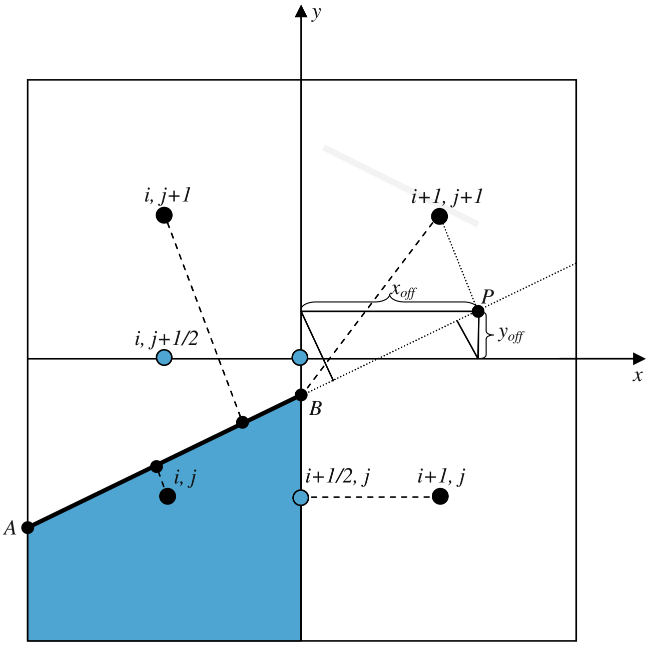

Fig. 4. Schematic for the LS function re-distance in two dimensions.

$$u(x) = \frac{U_R - U_L}{\Delta x}x + U_L = Ax + B, \tag{18}$$

where U_R and U_L are x velocity component on the two faces, $A = (U_R - U_L)/\Delta x$, $B = U_L$. Then the x coordinate of each point on the interface is updated to time $t^n + \Delta t$ with a second-order Runge–Kutta method,

$$x^{(*)} = \left[1 + A\Delta t + \frac{1}{2}A^2(\Delta t)^2\right]x^{(n)} + \frac{1}{2}AB(\Delta t)^2 + B\Delta t. \tag{19}$$

$x^{(n)}$ can be obtained from Eq. (19),

$$x^{(n)} = \frac{x^{(*)} - \left[\frac{1}{2}AB(\Delta t)^2 + B\Delta t\right]}{1 + A\Delta t + \frac{1}{2}A^2(\Delta t)^2}. \tag{20}$$

Eq. (20) is substituted into Eq. (17), the updated interface equation is obtained,

$$n_x^{(*)}x^{(*)} + n_y^{(*)}y^{(*)} + n_z^{(*)}z^{(*)} = \alpha^{(*)}, \tag{21}$$

where

$$n_x^{(*)} = \frac{n_x^{(n)}}{1 + A\Delta t + \frac{1}{2}A^2(\Delta t)^2}, \tag{22}$$

$$\alpha^{(*)} = \alpha^{(n)} + \frac{n_x^{(n)}\left[\frac{1}{2}AB(\Delta t)^2 + B\Delta t\right]}{1 + A\Delta t + \frac{1}{2}A^2(\Delta t)^2}. \tag{23}$$

Note that in the above equations, superscript $(*)$ is used rather than $(n + 1)$ to denote a fractional step, since the interface is just propagated in x direction at this stage. Eqs. (22) and (23) can be rewritten as follows, with $A = (U_R - U_L)/\Delta x$ and $B = U_L$ substituted,

$$n_x^{(*)} = \frac{n_x^{(n)}}{1 + \frac{Q_R - Q_L}{\Delta x}}, \tag{24}$$

$$\alpha^{(*)} = \alpha^{(n)} + n_x^{(*)}Q_L, \tag{25}$$

where $Q_L = (U_R\Delta t - U_L\Delta t)U_L\Delta t/(2\Delta x) + U_L\Delta t$ and $Q_R = (U_R\Delta t - U_L\Delta t)U_R\Delta t/(2\Delta x) + U_R\Delta t$. It is clear that Eqs. (24) and (25) will be reduced to the original first-order form (Gueyffier et al., 1999) if $\partial u/\partial x = 0$. After the interface is propagated in y and z directions through the same procedure, the interface is completely updated to time t^{n+1}.

3.3. LS re-distance

After the advection step, the LS function needs to be re-distanced in order to achieve mass conservation. Different LS re-distance algorithms can be found in (Bourlioux, 1995; Sussman and Puckett, 2000; Son and Hur, 2002; Son, 2003; Menard et al., 2007; Yang et al., 2007), which are mainly focused on the 2D examples, and details for 3D cases are not available. Although the schemes presented by Sussman and Puckett (2000) and Son and Hur (2002) can be extended to 3D cases, the procedure is complicated. The algorithm presented in this study significantly simplifies the complicated geometric procedure by finding the closest point on the reconstructed interface directly without considering the interface configuration in each computational cell with an interface.

The re-distancing of the LS function includes initial determination of the sign of the LS function and the subsequent calculation of the shortest distance from the cell centers to the reconstructed interface. The sign of the LS function, S^{ϕ}, is given by

$$S^{\phi} = sign(F - 0.5), \tag{26}$$

where *sign* denotes a function that returns the sign of the numeric argument. It is obvious that if $F > 0.5$, the cell center will fall inside the liquid where the LS function takes the positive sign, and vice versa.

Next, the magnitude of the LS function is determined, which is the most important step of the re-distancing process. The basic idea is to find the closest point on an interfacial cell to the neighboring cell centers. Although various configurations of the reconstructed interface exist, generally, all the computational cells can be simply divided into two cases: single-phase cells (i.e., $F = 0$ or 1) and interfacial cells (i.e., $0 < F < 1$) as discussed in Son and Hur (2002). For two adjoining cells (i,j,k) and (i',j',k'), the closest point on the boundary of cell (i,j,k) to the center of cell (i',j',k') will always be either at the corner or at the centroid of the cell faces (Sussman and Puckett, 2000; Son and Hur, 2002). Therefore, these points should always be considered first when calculating the shortest distance associated with two adjoining cells. When a cell contains an interface segment, for a 2D case, the closest point on the segment will be either one of the two endpoints or the projection point of the neighboring cell center. As for 3D cases, the recon-

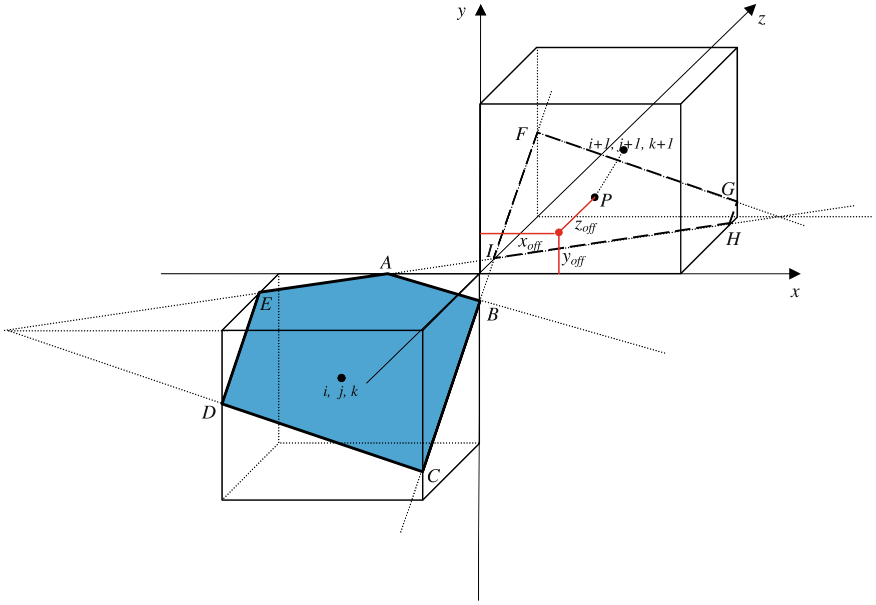

Fig. 5. LS function re-distance in three dimensions.

structed interface contained in the cell is an n-sided (from 3 to 6) polygon (see Fig. 2), the possible closest point on the polygon can be the projection point of the neighboring cell center to the interface, one of the vertices, and the projection point to one of the polygon sides from the neighboring cell centers. For example, as shown in Fig. 4, for cell $(i+1,j)$, the shortest distance is from the cell center to face centroid; for cells $(i,j+1)$ and $(i+1,j+1)$, the closest point is the projection point on the segment and the endpoint of the segment, respectively. The LS function re-distance procedure is given below, which includes the determination of which point is the closest point to the neighboring cells, and the corresponding calculation of the coordinates of that point.

For a given cell (i,j,k) with a reconstructed interface and its neighbor cell (i',j',k'), where $|i'-i| \leqslant K, |j'-j| \leqslant K$, and $|k'-k| \leqslant K$, K is the number of the computational cells within a narrow band (e.g., $K = 4$):

(1) The closest point V on the cell boundary is determined first. This point is either the face centroid or corner of the cell (Sussman and Puckett, 2000; Son and Hur, 2002). The coordinates $\mathbf{x}_V = (x_V, y_V, z_V)$ are given as $x_V = x_{i+l/2}$, $y_V = y_{j+m/2}$, and $z_V = z_{k+n/2}$, where $l = \max(-1, \min(1, i'-i))$, $m = \max(-1, \min(1, j'-j))$, $n = \max(-1, \min(1, k'-k))$. If $D(\mathbf{x}_V) * S^{\phi}_{i',j',k'} < 0$, then point V is the closest point to cell (i',j',k'), where $D(\mathbf{x})$ is the distance from point V to the reconstructed interface, which is given by

$$D(\mathbf{x}) = \frac{\alpha - (n_x x + n_y y + n_z z)}{\sqrt{n_x^2 + n_y^2 + n_z^2}} = \alpha - (n_x x + n_y y + n_z z), \qquad (27)$$

where $\sqrt{n_x^2 + n_y^2 + n_z^2} = 1$ according to Eq. (13).
For example, as shown in Fig. 4, the right face center of cell (i,j) is the closest point to the center of cell $(i+1,j)$.
If $D(\mathbf{x}_V) * S^{\phi}_{i',j',k'} \geqslant 0$, where point V and the center of cell (i',j',k') are in the same phase, e.g., for cells $(i,j+1)$ and $(i+1,j+1)$ in Fig. 4, then go to step (2).

(2) Find the projection point P of point (i',j',k') onto the interface, the coordinates $\mathbf{x}_P = (x_P, y_P, z_P)$ are determined by

$$\mathbf{x}_P = \mathbf{x}_{i',j',k'} + \mathbf{n} D(\mathbf{x}_{i',j',k'}). \qquad (28)$$

If point P falls inside of cell (i,j,k), $D(\mathbf{x}_{i',j',k'})$ will be the shortest distance. This is the case for cell $(i,j+1)$ in Fig. 4. As for the cell where point P falls outside of cell (i,j,k), then go to step (3).

(3) Find the closest point S on the boundary of interface segment. In this case, the closest point will be one of the two end points of the line segment for the 2D cases. As for the 3D cases, it can be one of the vertices of the n-sided polygon,

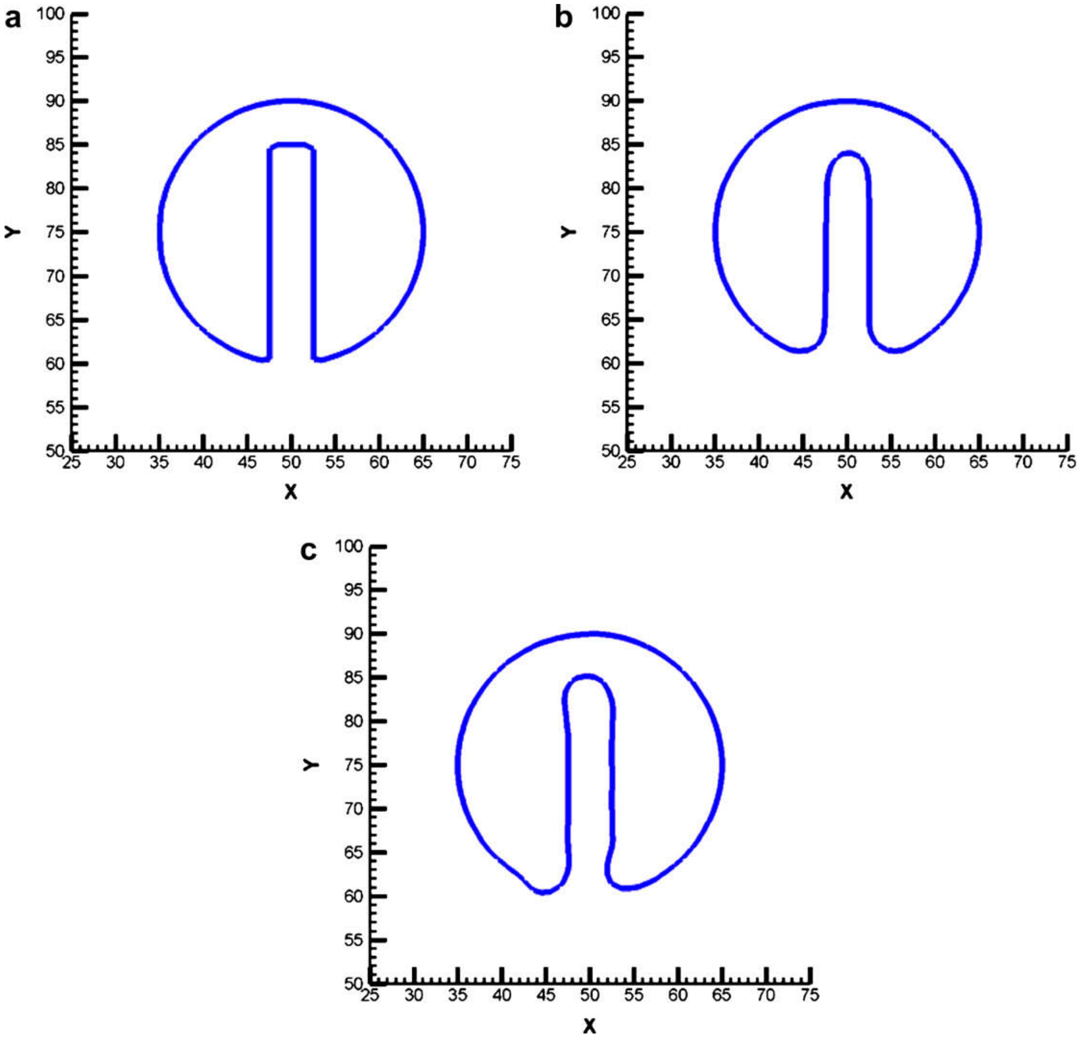

Fig. 6. Comparison of the solutions for different methods after one rotation of a slotted disk. (a) Initial shape; (b) LS; (c) CLSVOF. Grid: 100 × 100.

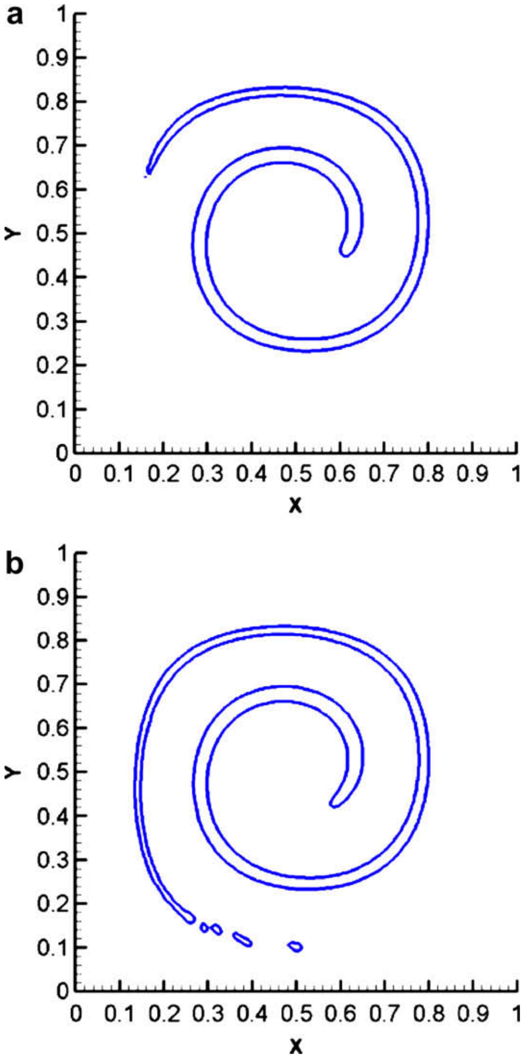

Fig. 7. Single vortex flow test at $t = 4$. (a) LS; (b) CLSVOF. Grid: 128 × 128.

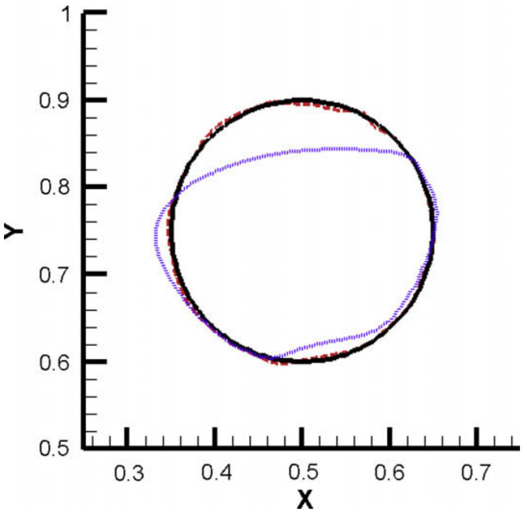

Fig. 8. Single vortex flow test at $t = 8$. Solid line: initial shape; dotted line: LS; dashed line: CLSVOF. Grid: 128 × 128.

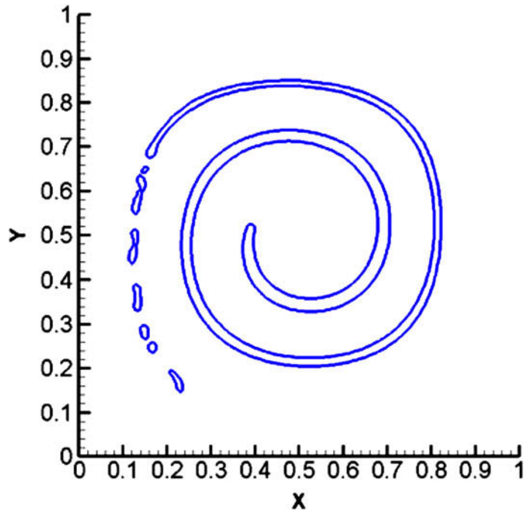

Fig. 9. Single vortex flow test without flow reversal at $t = 3$. Grid: 128 × 128.

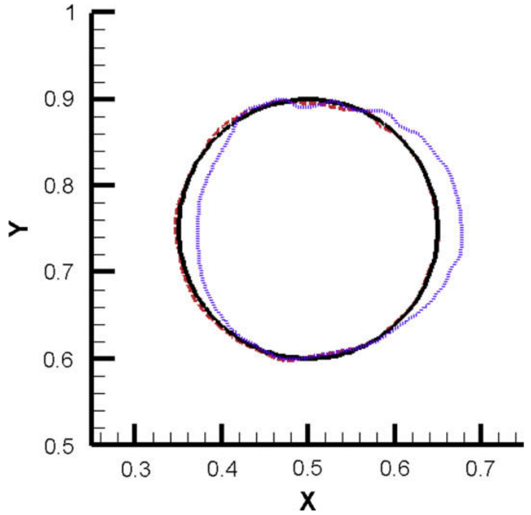

Fig. 10. Comparison of the recovered shapes with different interface propagation schemes. Solid line: initial shape; dotted line: first order; dashed line: second order. Grid: 128 × 128.

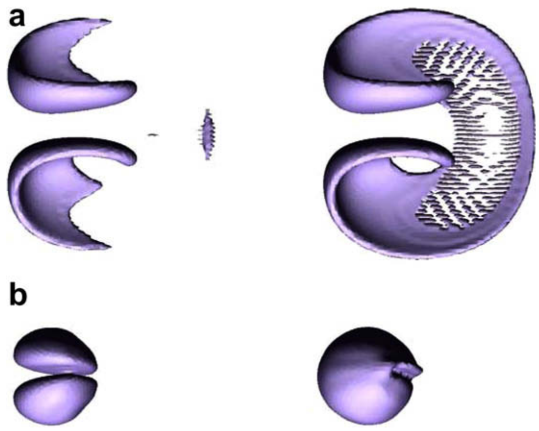

Fig. 11. Deformation of a sphere. (a) $t = 1.5$; (b) $t = 3.0$. Left: LS; right: CLSVOF. Grid: 100 × 100 × 100.

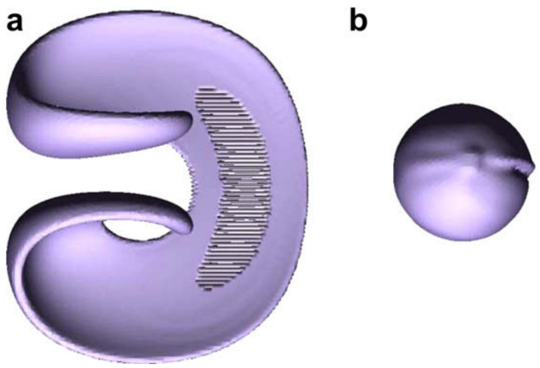

Fig. 12. Deformation of a sphere. (a) $t = 1.5$; (b) $t = 3.0$. Grid: 150 × 150 × 150.

Table 1
Relative mass errors of a deformed sphere.

Time	LS (100 × 100 × 100) (%)	CLSVOF (100 × 100 × 100) (%)	CLSVOF (150 × 150 × 150) (%)
$t = 1.5$	21.8	0.16	0.13
$t = 3.0$	32.1	0.40	0.27

or the projection point of neighboring cell center onto the side of the polygon. In the 2D algorithm presented by Son and Hur (2002), the distances to both of the two end points are calculated and compared to find the shortest distance. The same algorithm is used in Son (2003) with a procedure to determine the vertices of the interface segment given for the 3D cases. The procedure to find all the vertices of the polygon is complicated since five different interface configurations, as shown in Fig. 2, need to be considered. Moreover, for a 3D case, the projection point of point (i',j',k') onto the side of the polygon is also the possible closest point on the polygon boundary, which is not mentioned in the reference. Obviously, if all the possible closest points are determined and the distances are calculated, the procedure will be complicated and computationally expensive. In this study, a much simple and efficient procedure to locate the closest point on the interface boundary is presented below.

The auxiliary quantities, $\mathbf{x}_{off} = (x_{off}, y_{off}, z_{off})$ and $\mathbf{x}_{fc} = (x_{fc}, y_{fc}, z_{fc})$, are used to determine the coordinates, $\mathbf{x}_S = (x_S, y_S, z_S)$, of point S. $\mathbf{x}_{off} = (x_{off}, y_{off}, z_{off})$ is the distance that the projection point deviates away from the nearest boundary of cell (i,j,k) in each coordinate direction (see Figs. 4 and 5), given by

$$x_{off} = \max(|x_P - x_i| - 0.5\Delta x, 0), \tag{29a}$$
$$y_{off} = \max(|y_P - y_j| - 0.5\Delta y, 0), \tag{29b}$$
$$z_{off} = \max(|z_P - z_k| - 0.5\Delta z, 0). \tag{29c}$$

$\mathbf{x}_{fc} = (x_{fc}, y_{fc}, z_{fc})$ is the nearest face of cell (i,j,k) to the projection point, given by

$$x_{fc} = x_i + sign(x_P - x_i)0.5\Delta x, \tag{30a}$$
$$y_{fc} = y_j + sign(y_P - y_j)0.5\Delta y, \tag{30b}$$
$$z_{fc} = z_k + sign(z_P - z_k)0.5\Delta z. \tag{30c}$$

Find the $\max(x_{off}|n_x|, y_{off}|n_y|, z_{off}|n_z|)$, which is corresponding to the nearest face of cell (i,j,k) that is intercepted by the interface. For a 2D case as shown in Fig. 4, e.g., $x_{off}|n_x| > y_{off}|n_y|$, then set $x_S = x_{fc}$, and substitute it into the interface equation, y_S can be obtained immediately:

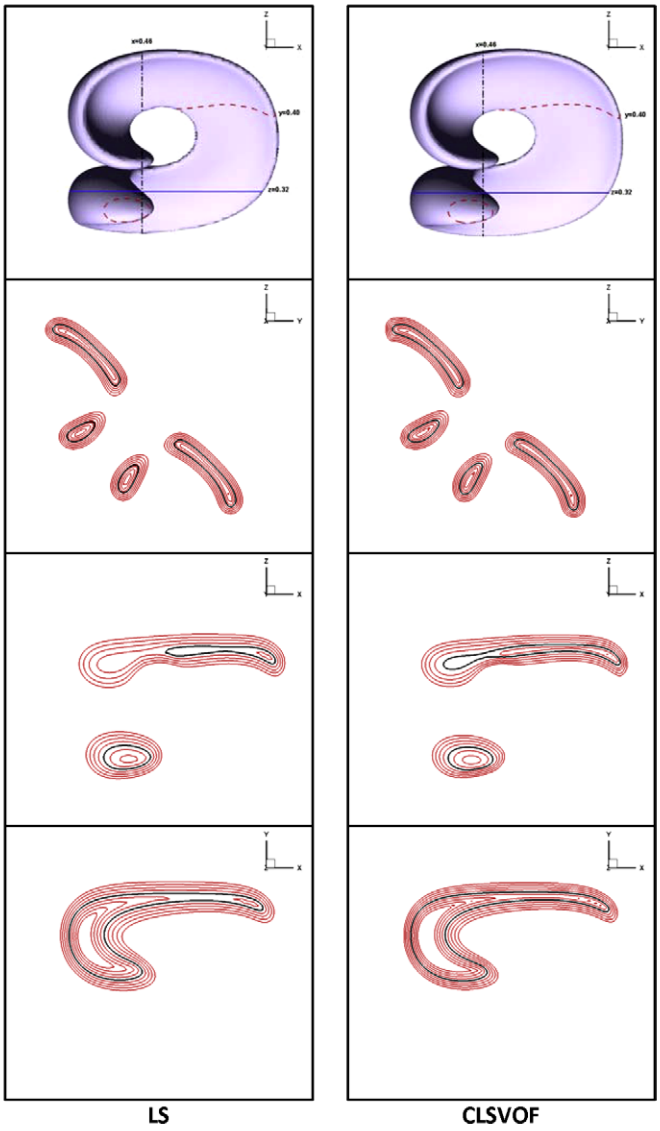

Fig. 13. Slices of the deformed shape in each coordinate direction at $t = 1.0$. Contour lines from −0.20 to 0.20.

$$y_S = (\alpha - n_x x_S)/n_y.$$

Thus point S (point B in Fig. 4) is found directly without considering the interface configuration. This will be especially efficient for 3D cases since it is not necessary to find all the vertices of the interface segment. For a 3D case (see Fig. 5), since $z_{off}|n_z| = \max(x_{off}|n_x|, y_{off}|n_y|, z_{off}|n_z|)$, then set $z_S = z_{fc}$ and substitution to the interface equation obtains:

$$n_x x + n_y y = \alpha - n_z z_S = \alpha'.$$

This reduces to a 2D problem, where x_S and y_S can be easily obtained by going back to step (2), and step (3) if necessary.

4. Advection tests

The CLSVOF method, along with the pure LS method, is first tested with prescribed velocity fields without solving the flow equations. The relative mass errors in all the following tests are within a fraction of one percent, which is comparable to those presented in Sussman and Puckett (2000).

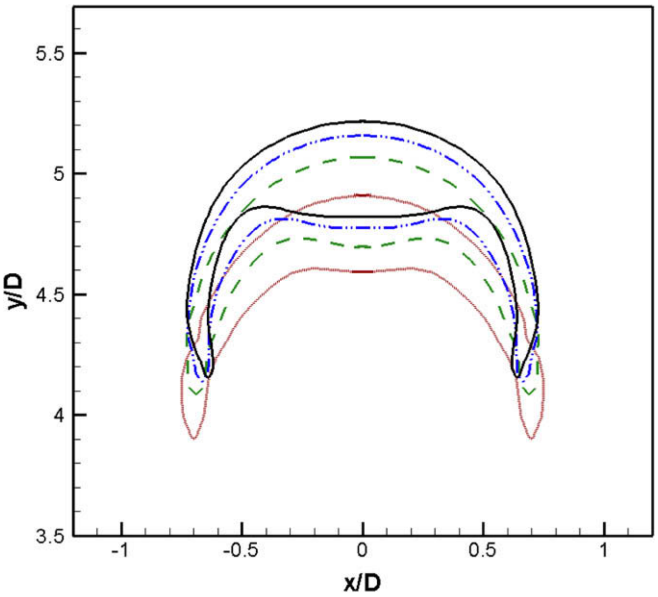

Fig. 14. Bubble shapes with different grid sizes. Dot line: coarse; dashed line: medium; dash-dotted: fine; solid line: finer.

4.1. Slotted (Zalesak's) disk

A slotted disc with a radius of 15.0 and slot width of 5.0 is initially located at (50.0,75.0) on a 100 × 100 computational domain. This problem, referred to as the Zalesak's problem, is often used for the interface modeling scheme test. The prescribed velocity field is given as:

$$\begin{aligned} u &= (\pi/314)(50 - y) \\ v &= (\pi/314)(x - 50) \end{aligned} \tag{31}$$

with the axis of rotation centered at (50.0,50.0).

The results after one rotation for both the LS and CLSVOF methods are shown in Fig. 6. Slight mass loss can be observed at the corners of the slot in the LS method. As for the CLSVOF method, mass is well conserved. The relative mass errors for the LS and CLSVOF methods are 0.13% and 0.0017%, respectively. In fact, for a solid body rotation, as in this case, both $\partial u/\ \partial x$ and $\partial v/\ \partial y$ are zero, the Lagrangian advection scheme can exactly conserve mass without numerical truncations. In the CLSVOF method, the edges at the corners of the disk slot are smeared and the symmetry is slightly lost. This is because a PLIC reconstruction scheme smoothes the regions with high curvatures, and the discontinuity near the corner will be progressively smeared out and advected faster in the rotation flow (Scardovelli and Zaleski, 2003). Since both $\partial u/\ \partial x$ and $\partial v/\ \partial y$ are zero, the second-order advection scheme discussed in the previous section performs the same as the original scheme used by Gueyffier et al. (1999).

4.2. Rider–Kothe single vortex flow

A circle evolving in a shearing flow is another challenging test for interface modeling schemes, which involves severe topological changes. The circle is stretched and torn in this vortex flow where very thin filaments on the scale of the mesh can be produced. A prescribed shearing flow is given by:

$$\begin{aligned} u &= (\sin(\pi x))^2 \sin(2\pi y) \cos(\pi t/T), \\ v &= (\sin(\pi y))^2 \sin(2\pi x) \cos(\pi t/T), \end{aligned} \tag{32}$$

where t is time, T is the time at which the flow returns back to its initial shape. A circle with a radius of 0.15 is prescribed at (0.5,0.75) on a computational domain of 1.0 × 1.0. The resulting velocity field stretches out the circle into a very long, thin fluid element which progressively wraps itself towards the center of the domain.

The results at $t = 4$ are shown in Fig. 7 where a maximal stretching is reached with T chosen as 8. It is clear that the CLSVOF methods well maintains the thin, elongated filament on the scale of the grid spacing, whereas serious mass loss occurs at both the head and the tail of the filament in the LS method. The relative mass errors for the LS and CLSVOF methods are 12.04% and 0.04%, respectively. Fig. 8 shows the results at $t = 8$ at which the flow field returns back to its initial state. The recovered shape in the CLSVOF method matches the initial shape very well with a relative mass error of 0.11%. As for the pure LS method, the recovered shape is far from a circle and mass is lost by 16.56%. The same case used in Menard et al. (2007) is also conducted and the results at $t = 3.0$ are shown in Fig. 9. Breakups of the filament at the tail can be observed in the present simulation and the mass loss is about 0.077%. The results in Menard et al. (2007) are closer to the solution obtained from Lagrangian method. It should be noted that it is difficult to reconstruct the interface with the PLIC scheme when the filaments of a thickness less than the grid spacing (Lopez et al., 2005). Special modification has been made to the interface reconstruction in Menard et al. (2007) for their purpose of modeling the breakup of a liquid jet, which is clearly suitable for this particular case (and the sphere stretching case). In a relevant study, Lopez et al. (2005) used markers on the reconstructed interface to track fluid structures thinner than the cell size. As mentioned previously, the primary objective of this paper is to develop the computational code with the capability for simulation details of wave breaking in ship hydrodynamics, which includes more general and complicated air/water interface interactions. Special treatment to resolve the thin fluid element less than the grid spacing is not indispensable.

For comparison purposes, the original first-order interface propagation scheme (Gueyffier et al., 1999) is also used in this test. The computed results at $t = 8$ are plotted in Fig. 10. A clear phase error is demonstrated in the first-order algorithm, this is because there is no implicit part in this scheme (Scardovelli and Zaleski, 2003). With a second-order interface propagation scheme, phase errors are avoided.

4.3. 3D deformation field

To demonstrate the ability of the CLSVOF method to capture 3D deformations, a 3D incompressible flow field which combines deformations both in the x–y and x–z planes is considered. The velocity field is given by

$$\begin{aligned} u &= 2\sin^2(\pi x)\sin(2\pi y)\sin(2\pi z)\cos(\pi t/T), \\ v &= -\sin(2\pi x)\sin^2(\pi y)\sin(2\pi z)\cos(\pi t/T), \\ w &= -\sin(2\pi x)\sin(2\pi y)\sin^2(\pi z)\cos(\pi t/T), \end{aligned} \tag{33}$$

where $T = 3$.

A sphere of radius 0.15 is placed within a unit computational domain at (0.35,0.35,0.35). A uniform grid of 100 × 100 × 100 is used. The sphere is stretched by two rotating vortices which initially scoop out opposite sides of the sphere and then reverse them back to the initial shape. The deformed shapes at $t = 1.5$ when it reaches the maximum stretching are shown in Fig. 11a, and the recovered shapes after the flow returns back are shown in Fig. 11b. As shown in Fig. 11a, the CLSVOF method partially resolves the thin interface film

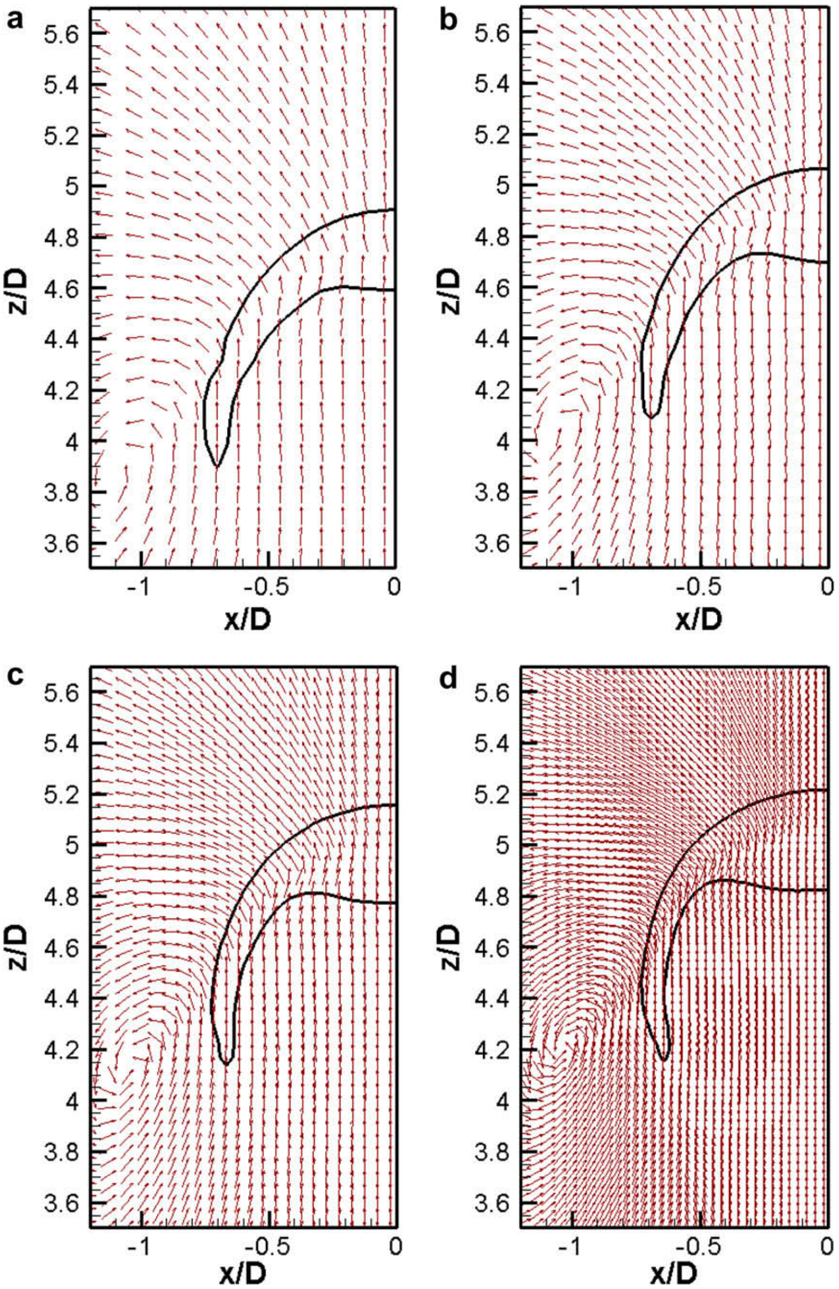

Fig. 15. Bubble velocity fields with different grid sizes. (a) Coarse; (b) medium; (c) fine; (d) finer.

produced at the middle section of the stretched shape. A better recovered shape is obtained in the CLSVOF method than the LS method as indicated in Fig. 11b. Fig. 12 shows the results computed on a fine grid of 150 × 150 × 150 which is the same as the case shown in Fig. 6 of Menard et al. (2007). As shown in Fig. 12a, grid resolutions are still not enough to resolve the thin membrane stretched at the center portion of the deformed shape. The relative mass errors for each case are given in Table 1. The results presented in Menard et al. (2007) are better since their method is designed for the jet breakup purpose as mentioned in the previous test.

Fig. 13 shows the slice of the deformed shape at $t = 1.0$ in each coordinate direction for both the LS and CLSVOF methods with the contour lines near the interface plotted. The results obtained from the LS and CLSVOF methods are very close, although the present re-distance algorithm in the CLSVOF method is completely different from the classic LS re-initialization. The contour lines are quite smooth and continuous, which demonstrates the capability of the re-distance algorithm presented in this study to reconstruct the LS functions in the 3D coordinates.

5. Verification and validation examples

5.1. Gas bubble rising in a viscous liquid

In this test, the CLSVOF method in conjunction with the flow solvers is applied to model a gas bubble rising in a viscous liquid. The key dimensionless parameters for this problem are the Reynolds number *Re*, the Eotvos number *Eo*, and the Morton number *M*, which are defined as follows:

$$Re = \frac{\rho_l DU}{\mu_l}, \quad Eo = \frac{\rho_l g D^2}{\sigma}, \quad M = \frac{g\mu_l^4}{\rho_l \sigma^3}, \tag{34}$$

where ρ_l is the liquid density, D is the bubble diameter, U is the bubble terminal velocity, μ_l is the liquid viscosity, σ is the surface

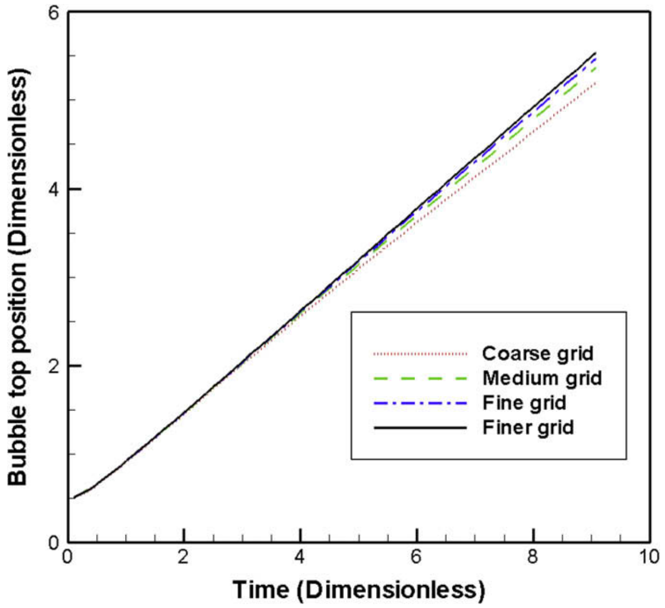

Fig. 16. Bubble top positions versus time with different grid sizes.

Table 2
Comparison of computed Reynolds number and the experimental measurement (Re = 18.3).

Grid	Re	Deviation (%)
$D/12$	15.90	13.14
$D/15$	16.83	8.01
$D/20$	17.35	5.17
$D/30$	17.74	3.09

tension coefficient, and g is the gravity acceleration. The physical properties (in terms of Eo number and M number) chosen here are the same as in Fig. 2(g) of the experimental study (Bhaga and Weber, 1981) with Eo = 339 and M = 43.1. As shown in the experiments (Bhaga and Weber, 1981), a skirted bubble shape is produced after the bubble reaches its steady state. It is a challenging test for the interface modeling method since the bubble undergoes severe shape deformations associated with the formation of a very thin skirt trailed behind the bubble. The computations are carried out on a $3D$ computational domain of $x = [-3.3D, 3.3D]$, $y = [-3.3D, 3.3D]$, and $z = [-3.3D, 8.0D]$. As discussed in Hua et al. (2008), when the domain size is beyond six bubble diameters, no significant change in the simulation results is observed. The wall confinement effect to the terminal velocity and shape can be neglected. Four different grids are used for the grid sensitivity study, where the number of computational cells in an initial bubble diameter is 12, 15, 20, and 30, respectively.

The predicted bubble shapes at $t = 8.51$ (time scale, $\sqrt{D/g}$) with different grid sizes are shown in Fig. 14. As shown in the figure, the edge of the bubble skirt tends to move towards the axis of the bubble from the coarse grid to the fine grid. This is because higher curvatures can be resolved with a finer grid. The relative mass errors for all the cases in Fig. 14 are 0.16–0.67%. Fig. 15 shows the corresponding velocity vector fields obtained on different grids. The position of the bubble top versus time plots with different grid sizes are given in Fig. 16. The computed rise velocity in terms of Reynolds number and the deviations from the experiment measurement are presented in Table 2. The terminal velocity on the finer grid is close to the experimental result (18.3) and agrees very well with the numerical value (17.76) calculated by Hua et al. (2008). Fig. 17 shows the computed $3D$ bubble shape ($t = 8.51$) compared with the experimental image (Bhaga and Weber, 1981) and the computational prediction using the front tracking method (Hua et al., 2008). The bubble shape obtained in the present study is closer to the experiment than the front tracking prediction. Both the experimental image and the present simulation show that the edge of the bubble skirt contracts inwards rather than opens up as in the front tracking method (Hua et al., 2008). The average thickness of the bubble skirt is approximately $0.083D$ in the present simulation.

5.2. Liquid drop impact

In the study by Morton et al. (2000), a 2.9 mm water drop impact on a deep water pool was simulated using the VOF method. It is a good example for interface modeling methods since it involves complicated flow deformations such as coalescence, air entrainment and jet formation. In this study, the experimental case with a falling height of 170 mm in Morton et al. (2000) is simulated, where the corresponding $Fr = 85$, $We = 96$, and $Re = 4480$. The simulation conditions are the same as those used in Morton et al. (2000) except that the current simulations are carried out on a fully 3D rather than a 2D axisymmetric domain. Details of the computational setup can be found in Morton et al. (2000).

Time sequences of the drop impingement process along with the video images and simulations presented by Morton et al. (2000) are shown in Fig. 18. The major events of the impact process, such as the formation of the vortex rings, entrapment of an air bubble during the cavity collapse and formation of the thin high speed liquid jet, are well captured in the current simulation. The predicted interface profiles also match both the experimental image and simulations very well. Due to the neglect of the gas phase dynamics in the numerical model used by Morton et al. (2000), the bubble could not be properly captured in their simulations. The cavity depths versus time are plotted in Fig. 19 with the results compared with both the experimental and numerical results presented by Morton et al. (2000). As shown in the figure, the present simulation agrees quite well with the numerical results at the early stage of the computations. Slight

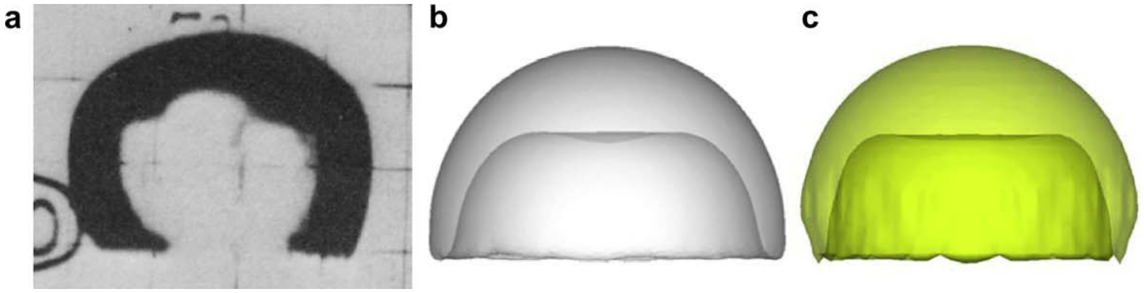

Fig. 17. Comparison of the bubble terminal shapes. (a) Experiment by Bhaga and Weber (1981); (b) simulation by Hua et al. (2008); (c) present simulation.

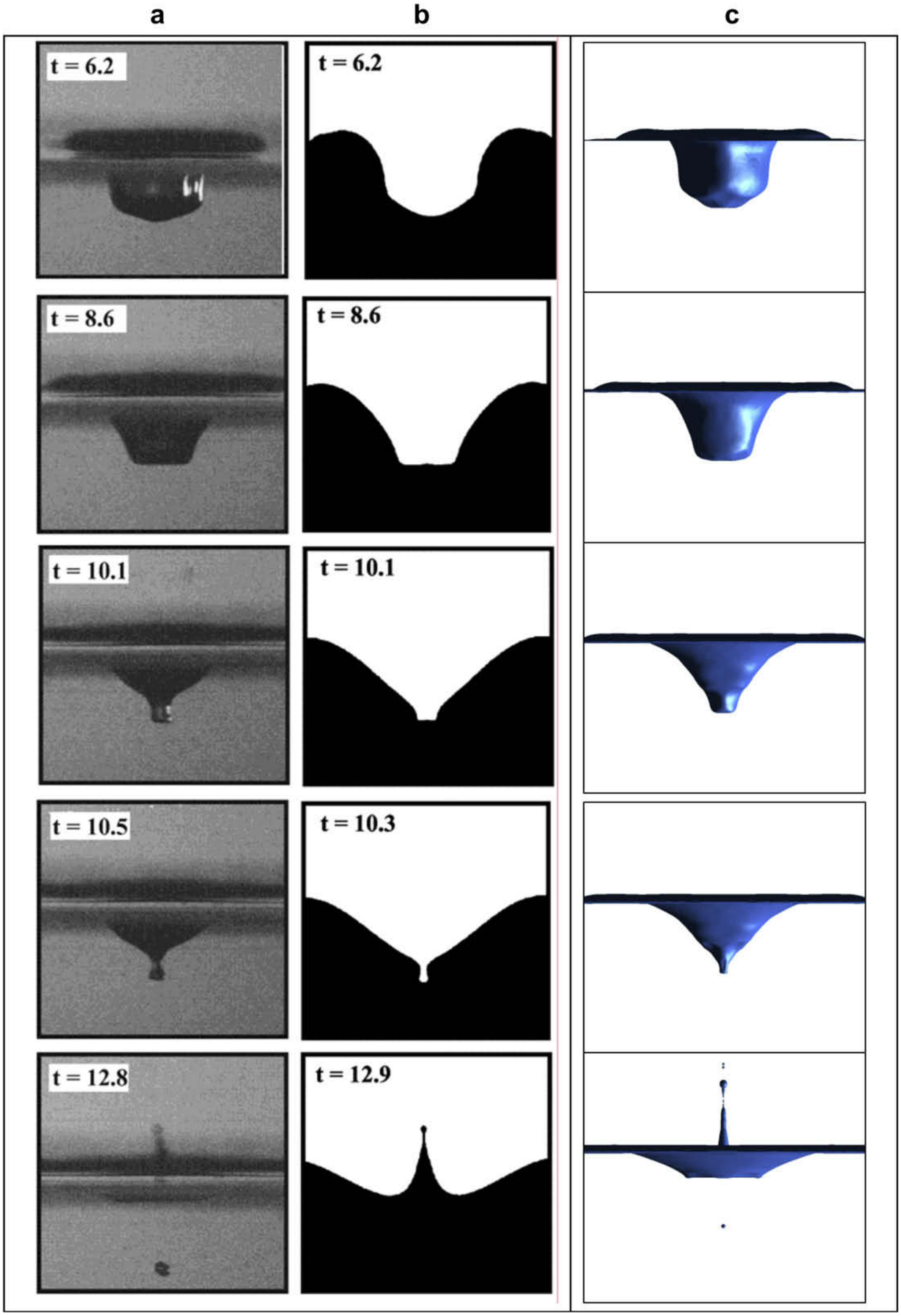

Fig. 18. Time sequences of a water drop impingement onto a deep water pool. (a) Experiment (Morton et al., 2000); (b) simulation (Morton et al., 2000); (c) present simulation.

oscillations of the depth can be observed at the later stage. This is likely due to the instability at the bottom of the cavity when it approaches maximum depth. Nevertheless, the averaged maximum depth still matches both the experimental and numerical measurements.

5.3. Wave breaking of a steep Stokes wave

Wave breaking of a steep Stokes wave (Chen et al., 1999) is simulated in this section. This case serves as a verification test of the accuracy of the code for the plunging wave breaking followed in

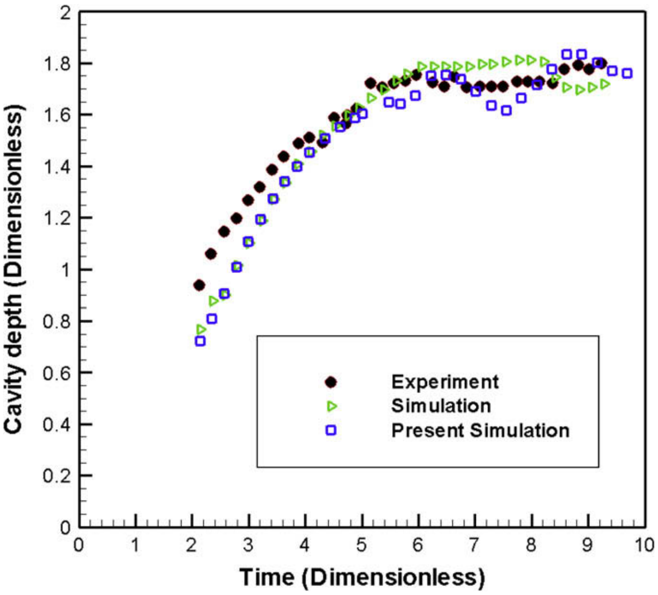

Fig. 19. Comparison of cavity depths of the experiments and simulations.

the next section. The computational conditions and physical parameters are the same as those used in Chen et al. (1999), details of the computational setup is not given herein. The snapshots of the time sequence of the wave breaking process are presented in Fig. 20. The wave breaking process shown in the figure includes the formation of the steep wave crest, overturning jet, wave plunging, air entrainment and splash-up. It is clear that the major wave breaking events are well reproduced in the present simulation, and the predicted wave profiles are in very good agreement with the simulation conducted by Chen et al. (1999). A little difference occurs after the wave plunges. This is likely because the surface tension model used in Chen et al. (1999) is different from the present study. During the wave overturning process at $t = 1.4$, the maximum velocity magnitude is about 0.827 which is very close to that reported in Chen et al. (1999).

6. Plunging wave breaking over a submerged bump

Wave breaking processes especially for plunging wave breaking are not yet well understood, including steep wave formation, jet overturning, splash-up, air entrainment, subsequent events, instabilities and organized vortices, and turbulence structures. Recent experimental fluid dynamics (EFD) and computational fluid dynamics (CFD) have focused on qualitative descriptions of the wave breaking process; energy losses; 2D and 3D vortex and turbulent structures; wave impact; air entrainment; surf zone modeling; and multi-scale turbulence model. The most relevant previous experimental and computational studies on plunging breaking wave process and velocity and turbulence flow fields can be found in the studies (Peregrine, 1983; Bonmarin, 1989; Tallent et al., 1990; Melville et al., 2002; Chang and Liu, 1999; Toomas, 2001; Watanabe et al., 2005). A complementary experimental and computational study of plunging breaking waves generated in an open channel flume using a bottom bump and impulsive accelerated flow was presented by Ghosh et al. (2007). The geometry is of particular relevance to ship hydrodynamics, since the breaking involves body–wave interactions. The experiments were carried out in an open channel flume (9 m long, 0.6 m wide, and 0.43 m high). The time evolution of the transient wave and its flow properties were measured using EFD: upstream and downstream velocity and flow rates using pitot probes; air–water interface elevation measurements and 2D particle image velocimetry (PIV) in the wave breaking region. The side and plan views of the experimental setup are shown in Fig. 21a and b. The figures show the flume to scale with the bump fixed at the flume bottom. Cartesian coordinate system is used where, x is the stream-wise direction, y is the span-wise direction and z is the vertical direction. The bump center is placed at $x = 0$ and $z = 0$ and the flume center plane is at $y = 0$. All length scales are normalized using the bump height ($H = 0.1143$ m), unless otherwise mentioned. The flume is connected to two pumps each of 7.5Hp rating. The objective was to suddenly accelerate the fluid from zero to maximum velocity in the shortest time to replicate the impulsive start flow conditions as closely as possible and also create waves of maximum height. To achieve this both pumps are run simultaneously to attain maximum pump power. Each pump is controlled by a frequency driver where the pump speed is set using a frequency scale of range 0–60 Hz. After setting the initial stationary water depth $\zeta = 2$, the pumps are primed by vacuuming out any entrapped air in the areas of the pump lines that are above the flume water surface. The flow is accelerated from zero to a pump setting of 55 Hz within 7 s which corresponds to a mean upstream velocity of 0.39 m/s at the time of breaking. The flume has two pipes underneath the channel and each pipe is connected to each pump. The flow in the channel is from left to right while in the pipes it is from right to left as highlighted by the arrow in Fig. 21a. More details of the experimental setup can be found in Ghosh et al. (2007) and Ghosh (2008). The CFD study of the plunging wave breaking is presented here with a focus on the wave breaking process. Since strong water/air interactions are involved during the wave breaking process, it is a very challenging case for interface modeling method.

The numerical simulations are conducted on a 2D computational domain of $x = [-52,44]$ and $z = [0,5]$, with a grid size of 768×256. The boundary conditions and the non-uniform grid structure are given in Fig. 22. A sharp interface immersed boundary method (Yang and Balaras, 2006) is adopted here to treat the immersed bump. The inlet velocity imposed at the left boundary is $U = 0.87$ m/s for water and zero for air. The initial free surface elevation is $\zeta = 1.85$ and a uniform velocity field of 0.87 m/s is prescribed in the water domain at $t = 0$ with the air phase at rest. The corresponding Reynolds number, $Re = \rho_l UH/\mu_l$, is 99441 and Froude number, $Fr = U/\sqrt{gH}$, is 0.82 based on the bulk inlet velocity and the bump height ($H = 0.1143$ m). Ghosh (2008) performed phased average experiments 7 times (about 24 individual tests for each phased average), but with limited documentation of overall flume flow (upstream/downstream wave elevations, velocities, and venturi flow rates). Present CFD is contemporaneously with the experimental study of Ghosh (2008) and is used to guide and analyze EFD. In the experiments, the flow is transitional and completely impulsive and wave breaks during the flow acceleration process. The experimental flow conditions are complicated and hence are difficult to model, for simplicity, constant inlet flow condition is used in the computations. The initial and inlet velocity and free surface elevation are chosen based on the sensitivity study conducted in Ghosh et al. (2007) in order to match wave breaking location in the EFD. Reins (2008) recently performed three additional phase averaged experiments for the same experimental setup as Ghosh (2008), including detailed documentation of the overall flume flow. These EFD data along with those obtained by Ghosh (2008) will be used for gradual acceleration conditions in the future investigations. The time step initially is 5×10^{-5} and then is reduced to 1×10^{-5} after the flow becomes violent due to wave breaking.

Calculations are performed on three different grids with consecutively reduced (by a factor of $\sqrt{2}$) sizes from 1088×352 to 768×256 and 544×176 for grid sensitivity study. Computational

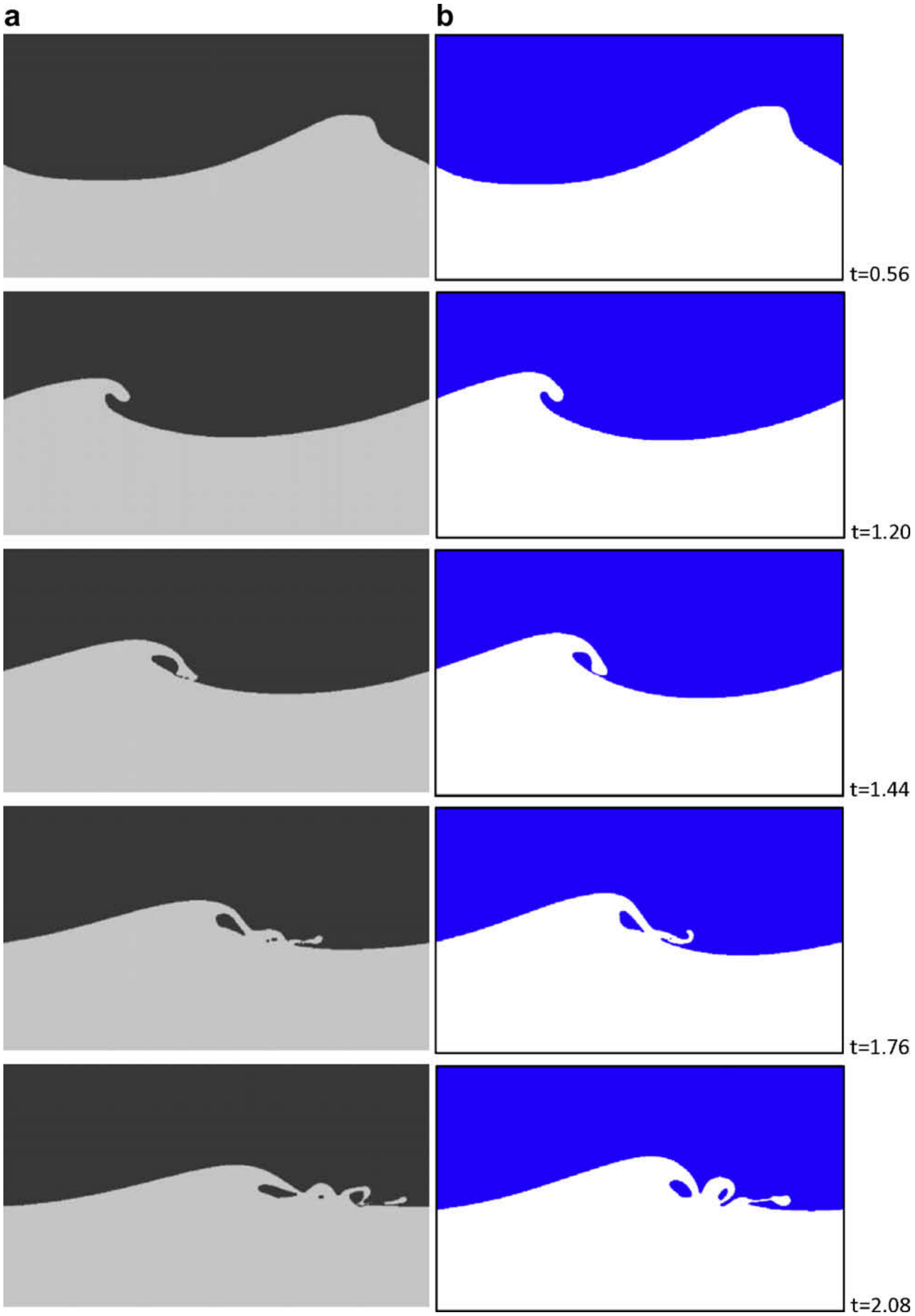

Fig. 20. Snapshots of the time sequence of a plunging breaking wave. (a) Simulation by Chen et al. (1999); (b) present simulation.

results on the three grids are shown in Fig. 23, which only shows the jet overturning process. The overall structures of the interface obtained on the three grids are similar. The jet tip is much thinner and sharper on a fine grid than on a coarse grid since a fine grid can capture more details of the interface structure with higher grid resolutions. As discussed in Lubin et al. (2006), grid convergence analysis is quite difficult and questionable for this kind of flow which is characterized by unsteady air/water interface breaking. Although much smaller interface structures can be resolved with higher grid resolutions, the overall large scale dynamics of wave breakings are not affected by the small interface structures. The grid with a medium size is used in the following simulations.

The time sequences of wave breaking process computed using both the LS and CLSVOF methods are given in Fig. 24. The time is non-dimensionalized by the time scale H/U, where U is the inlet velocity for CFD and mean upstream velocity for EFD. As will be discussed later, the major events in the wave breaking process are maximum wave height, first plunge, oblique splash, vertical jet, repeated processes, chaotic motions and broken wave swept downstream. At the early stage of the computations, the general structures of the wave profile are very similar. The maximum wave height ($t = 0$) and the first jet plunge ($t = 1.75$) are well demonstrated in both methods. After the jet hits the trough surface ($t = 2.82$), an oblique splash-up with many small droplets can be found in the CLSVOF method, this is in agreement with the experimental findings. As for the LS method, the oblique splash-up is not properly captured. The vertical jet reaches its maximum height ($t = 4.80$), which can be seen in both methods. In the subsequent

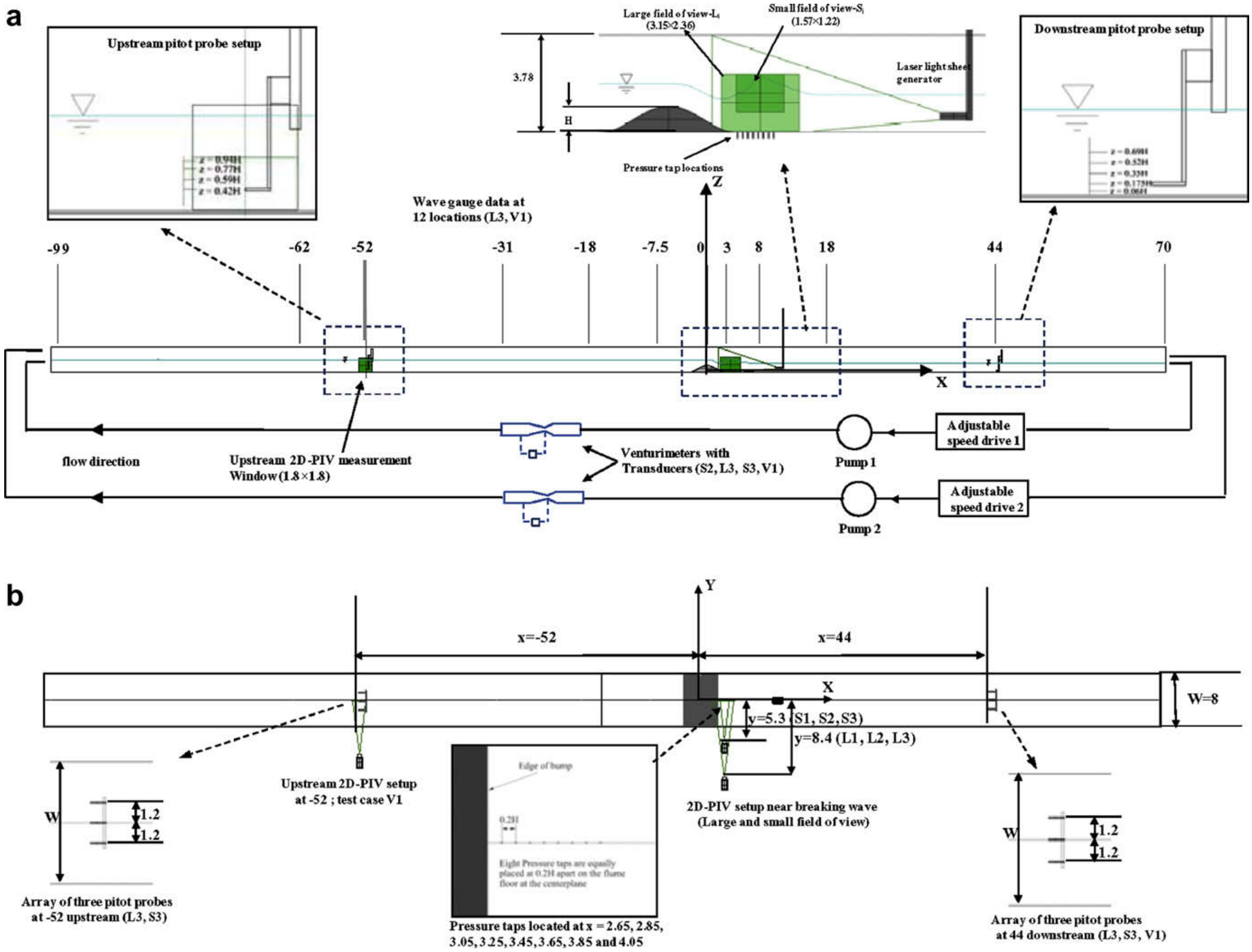
a
Upstream pitot probe setup
z = 0.94H
z = 0.77H
z = 0.59H
z = 0.42H
Large field of view-L1 (3.15×2.36)
Small field of view-S1 (1.57×1.22)
3.78
H
Laser light sheet generator
Pressure tap locations
Downstream pitot probe setup
z = 0.69H
z = 0.52H
z = 0.33H
z = 0.175H
z = 0.06H
Wave gauge data at 12 locations (L3, V1)
Z
-99
-62
-52
-31
-18
-7.5
0
3
8
18
44
70
X
flow direction
Upstream 2D-PIV measurement Window (1.8×1.8)
Venturimeters with Transducers (S2, L3, S3, V1)
Pump 1
Pump 2
Adjustable speed drive 1
Adjustable speed drive 2
b
Y
x=-52
x=44
X
W=8
y=5.3 (S1, S2, S3)
y=8.4 (L1, L2, L3)
W
1.2
1.2
Array of three pitot probes at -52 upstream (L3, S3)
Upstream 2D-PIV setup at -52 ; test case V1
Edge of bump
0.2H
Eight Pressure taps are equally placed at 0.2H apart on the flume floor at the centerplane
Pressure taps located at x = 2.65, 2.85, 3.05, 3.25, 3.45, 3.65, 3.85 and 4.05
2D-PIV setup near breaking wave (Large and small field of view)
Array of three pitot probes at 44 downstream (L3, S3, V1)

Fig. 21. Schematic of the experimental setup. (a) Side view. The upstream and downstream pitot probe arrangements are shown in close-up views. The close-up of the 2D PIV measurement areas near the wave breaking region is also shown. (b) Top view.

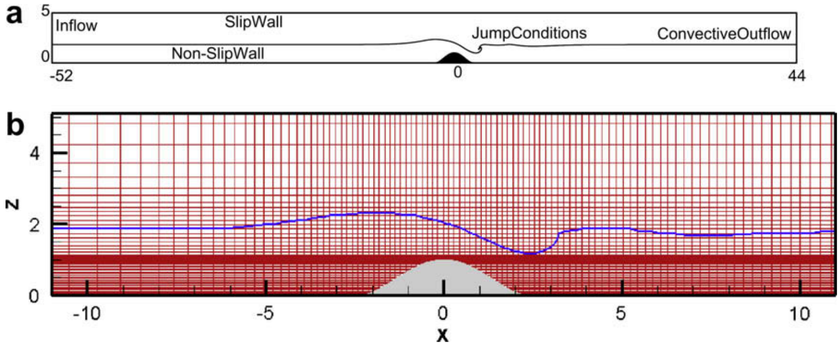

Fig. 22. Computational domain and grid structure for wave breaking over a submerged bump. (a) Computational domain; (b) grid structure.

events ($t = 6.01$–8.14), the CLSVOF method shows the second plunge, oblique splash-ups and vertical jet, and the third plunge at last. In LS method, however, only the second jet plunge is indicated after which the flow appears to enter a chaotic motion of air and water. Moreover, in the entire wave breaking process, small scale droplets and air bubbles can hardly be found in the LS method. The CLSVOF method is likely more suitable for modeling the wave breaking phenomenon, since it is able to capture more details of the wave breaking events.

The plunging wave breaking process has been characterized in the previous studies (Peregrine, 1983; Bonmarin, 1989; Tallent et al., 1990) by four major phases including steep wave formation, jet formation and overturning, splash-up and air entrainment as summarized in Table 1 in Ghosh et al. (2007). The first two phases, i.e., steep wave formation and jet overturning, are very similar in most experimental and numerical studies even though the flow conditions and the mechanism that induces wave breaking are different. However, the subsequent phenomena after the jet overturn-

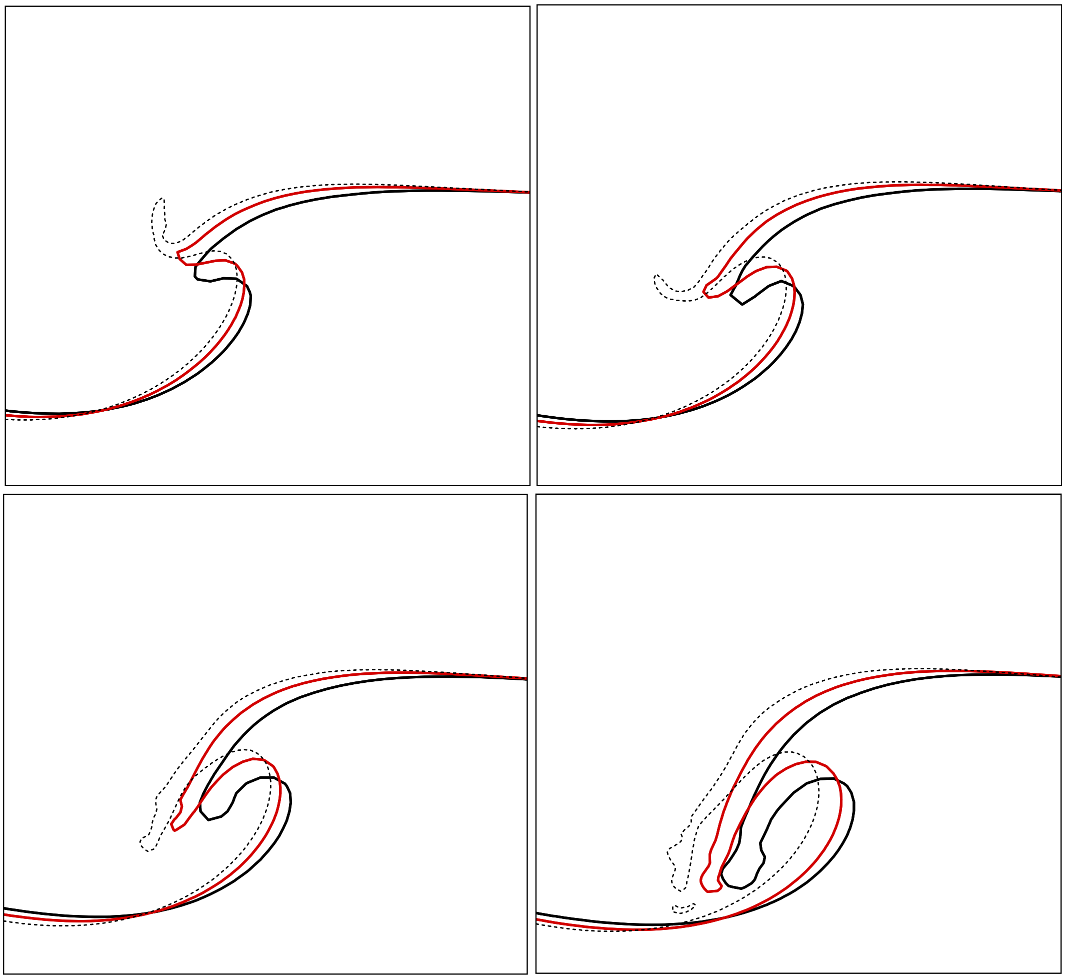

Fig. 23. Comparison of three different grids: coarse grid (black solid line), medium grid (red solid line), fine grid (black dotted line). (For interpretation of the references to colour in this figure legend, the reader is referred to the web version of this paper.)

ing observed in the above studies vary considerably. The angle of the overturning jet just prior to the plunge varies with different studies, while the surface profile beneath the jet is approximated with the similar elliptical shape. After the jet hits the trough surface, the splash-up angles are different for different studies, and different researchers have different opinions about the origin of the splash-ups. Most of the previous studies have reported occurrence of successive splash-up cycles with reduced energy after the first plunge and the degeneration of the flow into a chaotic motion.

Herein, wave breaking is triggered by the flow over a submerged bump which differs significantly from the previously mentioned experimental studies regarding flow conditions, jet overturning directions and subsequent events. The following major events in the plunging wave breaking process have been identified: maximum wave height, first plunge, oblique splash, vertical jet, two repeated processes, chaotic motions and broken wave swept downstream as shown in Fig. 24. Fig. 25 summarizes the overall PIV results (close-up views) in the wave breaking region and its comparison with CFD at various time steps that describe the most important events in the wave breaking process. Video images of the plunging breaker with reference scales are presented in column 1. PIV images with overlaid 2D CFD air–water interface profiles are shown in column 2. t_b is a reference time at which the wave reaches its maximum height, which is chosen as the initial time in Fig. 25 for comparing experimental and numerical results. The CFD air–water interface profiles were initially studied to identify the overall wave breaking process and its major events. Subsequently, those events were also identified qualitatively from the video and PIV images in EFD. In the current layout of Fig. 25, the EFD and CFD results are compared side by side for those particular events and hence the time instances do not necessarily match due to the differences in the initial conditions. Although the CFD time is given in the CFD U contour plot, unless otherwise specified, the EFD time is always referred to in the discussions.

At time $t = 0$ the wave crest becomes steepest when it reaches its maximum height. As the wave crest starts to overturn the steep angle θ_E, defined as the angle between the horizontal free surface and the jet's longitudinal axis, also increases, and its edge breaks into some small droplets in air. At the instant just prior to the first plunge, the CFD steep angle is approximately 50 degrees which is less than the EFD value. At $t = 0.22$, the first plunge occurs when the overturning jet impinges onto the free surface of the trough. The θ_E increases to approximately 75 and 85 degrees in the CFD and EFD profiles, respectively, compared to the previous time step. With the overturning jet, a large amount of air below the jet is entrapped which forms a big air bubble. The entrapped air bubble can also be observed in the PIV image at $t = 0.22$. The size of the air bubble in CFD is almost 2.0 times larger than the EFD. The CFD results show that the entrapped air bubble initially resembles an ellipse with an axis ratio of 2.153 which is slightly larger than those (usually, $\sqrt{3}$) found in the EFD

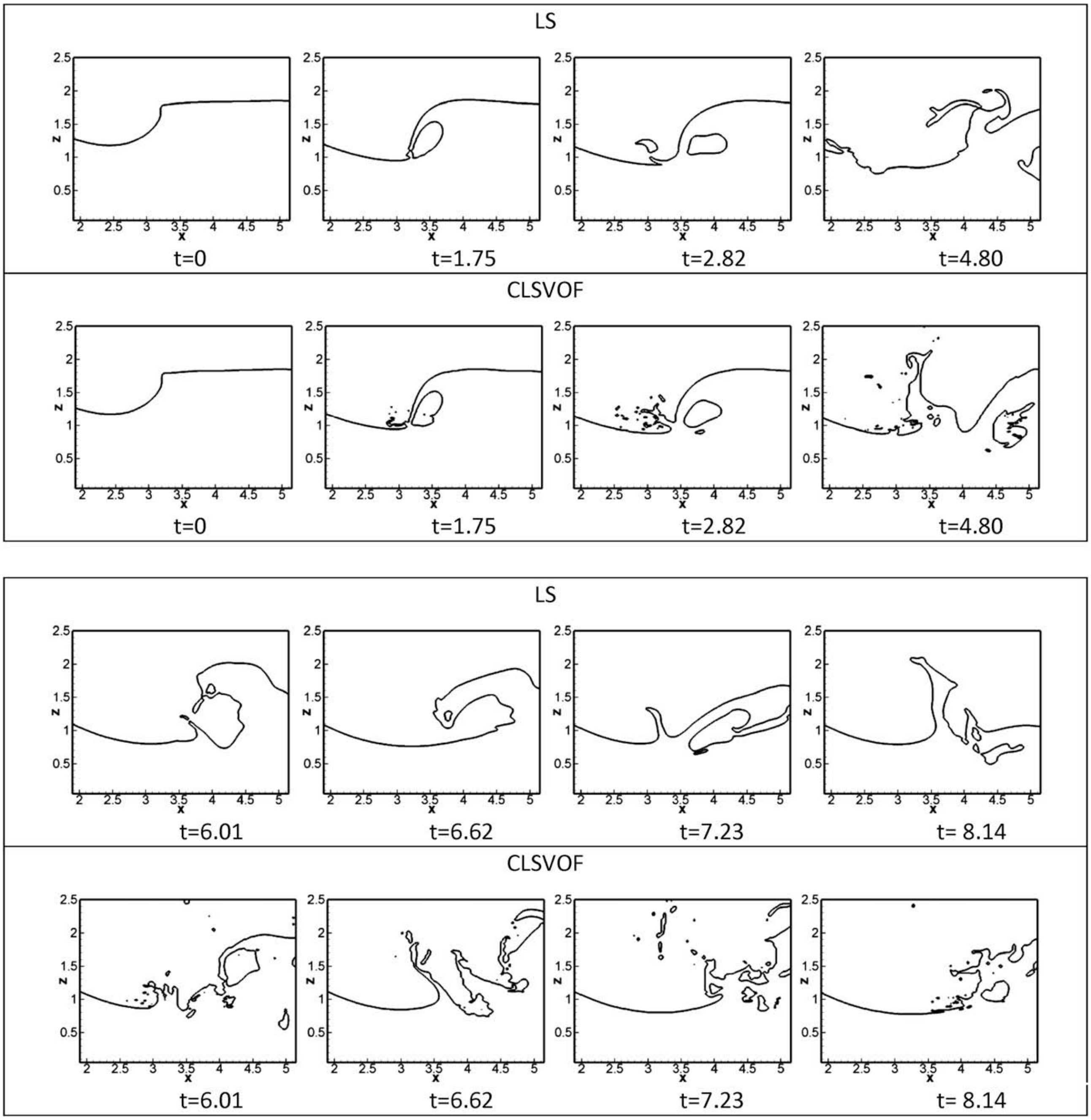

Fig. 24. Instantaneous free surface profiles of the wave breaking process.

and previous studies. Once the jet tip touches the trough surface, splash-up initiates and develops at the location where the jet impacts. At $t = 0.67$ as shown in CFD plot, an oblique splash-up is generated towards the upstream direction with a spray region. This spray region is more clearly shown in the experimental video image. The PIV image also shows that the red (the color indicates bubble concentration) region intensifies. This oblique splash-up appears to “rebound” from the overturning jet rather than originates from the trough surface, which can be clearly seen from the CFD velocity vector field. The splash-up intensifies and a vertical jet can be clearly observed in the CFD profiles with its maximum height of $\zeta = 2.15$ at $t = 1.12$. The video image shows the spray zone grows in size with more intense splash-up reaching a maximum height of $\zeta = 2.22$. In between $x = 2.2$ and $x = 3.6$ the broken wave creates an aerated region. A vertical jet can also be observed at $x = 3.0$ that is ejected from the trough. The CFD velocity vector field shows that the fluid of vertical jet mainly comes from the disturbed trough surface. After the first wave plunge, the splash-up initially originates from the plunging crest which forms an oblique spray and intensifies with more water coming from the trough. This agrees with the explanation (Tallent et al., 1990) on the origin of the splash-ups. The initially entrapped air bubble eventually breaks up at around $t = 1.34$ (not shown here). Severe bubble shape deformations can be seen in the CFD plot as it moves downstream. As the vertical jet decreases in height, another jet is formed which starts to initiate the second plunge, followed by the second oblique splash-ups and the second vertical jet. After the third jet impacts onto the trough surface, multiple small scale splash-ups and plunges keep occurring, and finally the broken wave is swept downstream leaving a trail of aerated region. Two repeated processes are observed in the present CFD

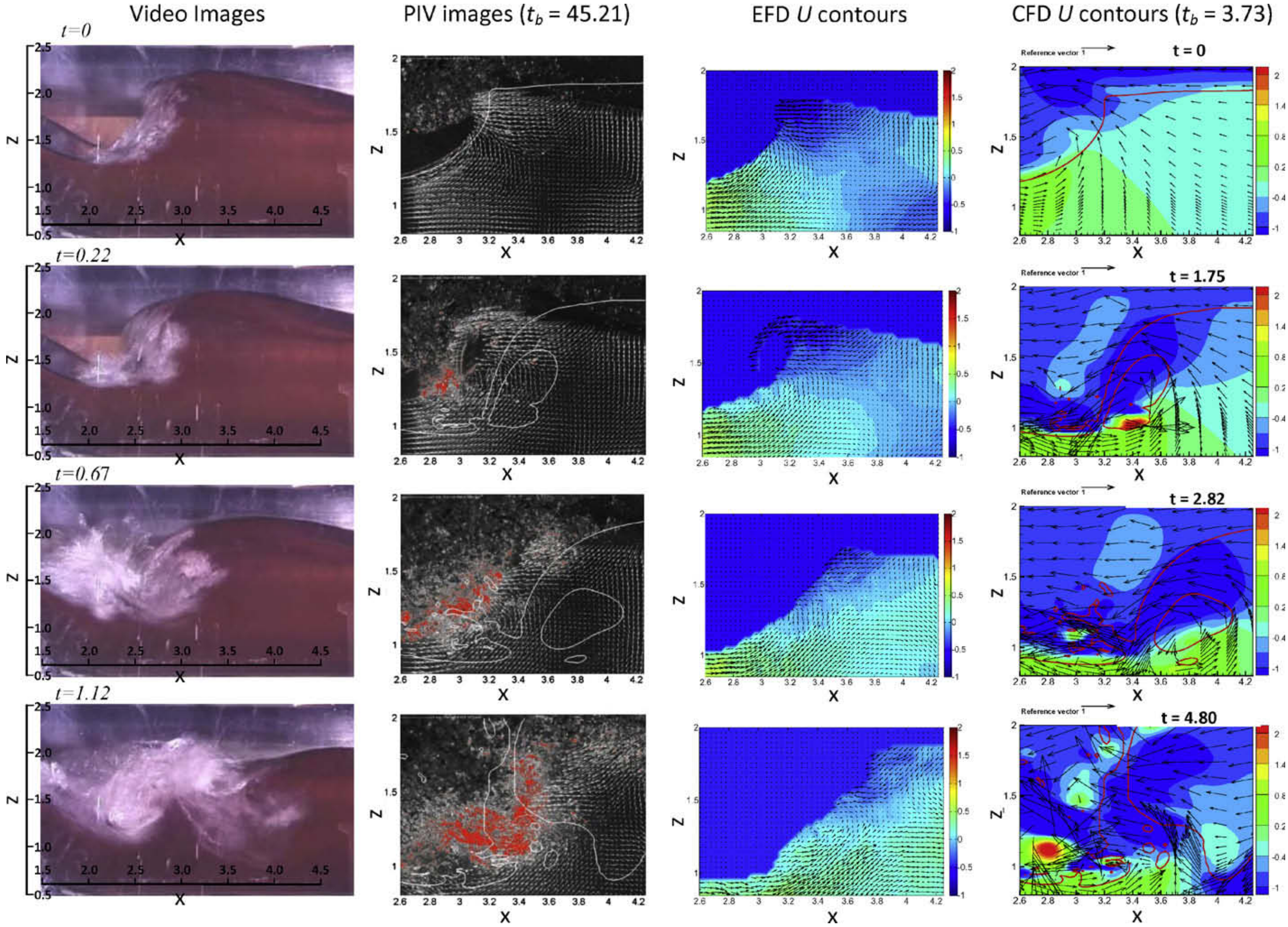

Fig. 25. Impulsive breaking waves behind a bump. From left to right: video image; PIV image with overlaid CFD wave profile; EFD U contours and CFD U contours.

results, in the recent EFD study by Reins (2008), four repeated processes are identified. The number of repeated processes likely depends on the acceleration flow conditions.

The CFD profiles show that the wave breaking occurs further downstream compared to the EFD profiles, which is clearly seen in the first and second plunging events. This is likely because the initial mean flow velocity is higher in the CFD simulations. It is found that the entrapped air bubble after the first plunge collapses in EFD, but remains intact in CFD. This may be because of 3D instability, which can contribute to the relatively short life of the air bubble (Peregrine, 1983) that does not exist in the 2D simulations. A clear two-phase (aerated) region is demonstrated in the experimental video images after the jet overturning. However, it is hard to define an exact two-phase region for the 2D simulations. Since the interface is modeled via an interface tracking method which is not able to capture air bubbles or droplets at the scale less than the grid spacing, a mixture model is needed in order to properly simulate the aerated region in future investigations.

The third and fourth columns of Fig. 25 show the EFD U contours and the CFD U contours, respectively, at the time steps that correspond to the wave breaking process with the velocity vectors overlaid on top. All contour plots and velocity vectors are presented in dimensional form. All EFD data is ensemble averaged and CFD data is instantaneous. The mean stream-wise velocity component within the water phase of the display area at each time step has been subtracted from the vector fields for both EFD and CFD. To be consistent with the vector representation the mean stream-wise velocity has also been subtracted from the background contours. The CFD velocity vectors of column 4 are of the same magnitude as the EFD vectors of column 2 and not the vectors in column 3 whereas, the EFD velocity contours in column 3 are of the same scales as the CFD velocity contours of column 4. Even though the CFD simulations were conducted for a much larger domain size, in the present layout the CFD x and z limits are matched with the EFD scales for comparison. At time $t = 0$, the EFD results show a positive U region extends towards downstream with the magnitude reduced in the region where steep wave is formed. A negative U region in the crest initiates and intensifies after the first plunge. For $0 \leqslant t \leqslant 1.12$, the positive U region moves towards downstream with the magnitudes continuing to increase, the EFD results show resolvable details of steep wave formation, first plunge, oblique splash and the vertical jet. Similar flow trends can be found in CFD U contours, with more detailed resolutions of plunging, splashing, vertical jet and bubble entrainment events in the wave breaking region. The impingement of the jet onto the free surface induces strong air flows as shown in the CFD U contours, which result in a pair of positive vortices immediately before jet. After falling jet impacts onto trough surface and the splash-up moves upwards, a series of vortices are generated and air flow turns to be stronger because of splash-ups and vertical jet. In the EFD, a clockwise rotating span-wise vortex is found to be shed from the bump and convected in the vertical direction by the rising fluid and also in the downstream direction by the mean flow. This bump vortex cannot be observed in the CFD results, this is due to the differences in the impulsive start conditions. The wave breaking vortex is clearly demonstrated in the CFD vorticity plot (not shown here) as part of plunging and bubble entrainment events.

7. Conclusions and future work

The CLSVOF method has been implemented in order to improve the mass conservation property of the LS method. The interface is reconstructed via a PLIC scheme and the LS function is re-distanced based on the reconstructed interface. The interface is advected using a Lagrangian method with a second-order Runge–Kutta scheme for time integration. A LS re-distance algorithm is developed, which significantly simplifies the complicated geometric procedure by finding the closest point on the reconstructed interface directly without considering the interface configuration in each computational cell. It is especially efficient for 3D cases where various possibilities of the interface configuration exist. The performance of the CLSVOF method has been evaluated through the numerical benchmark tests and verification and validation examples, where mass conservation has been well preserved.

The computed results of a gas bubble rising in a viscous liquid are compared with the available numerical and experimental results, and good agreement is obtained in terms of the predicted bubble shape and bubble rising velocity. In the test of a water drop impact onto a deep water pool, details of the drop impingement process, such as formation of the vortex rings, air entrainment and rebounding liquid jet are captured in the CLSVOF method. The numerical results match both the available experiments and simulations very well. Wave breaking of a steep Stokes wave is also modeled and the results are very close to the numerical results available in the literature.

The CLSVOF method is applied to simulate plunging wave breaking over a submerged bump, and the computational results are compared with the complementary EFD data. The major wave breaking events are identified from the CFD results and are qualitatively confirmed by the EFD findings. CFD studies reveal that the major events at the early wave breaking stage, such as maximum wave height, first plunge and splash-ups are similar to the observations reported in the literature. Subsequent events are examined and some distinct wave breaking events, such as vertical jet formation, two (even more) repeated processes with reduced amplitudes, chaotic motions and broken wave swept downstream, are identified in the later wave breaking stages. The number of repeated processes likely depends on the acceleration flow conditions. CFD results suggest that the first oblique splash-up appears to rebound from the overturning jet, whereas the first vertical jet originates from the disturbed trough. The flow structures are also compared with the EFD data qualitatively, similar flow trends have been observed in the CFD results. Due to the different initial flow conditions used in the CFD, bump vortex observed in the EFD cannot be found in the CFD.

For the plunging wave breaking, further investigations using the gradual acceleration conditions based on EFD will be made in order to quantitatively validate the CFD results. A fully 3D large eddy simulation (LES) including surface tension is necessary for a better understanding of the physics of the plunging wave breaking phenomenon. In order to further validate the CLSVOF method, more test cases, such as spray sheet formation and breakup induced around a ship bow, will be investigated in the future work.

Acknowledgements

This work is sponsored by the US Office of Naval Research through research Grants N00014-01-1-0073 and N00014-06-1-0420 under the administration of Dr. Patrick Purtell. The numerical tests and simulations were performed using DoD HPC resources. The authors would like to thank Dr. Tao Xing for his comments in preparing this manuscript, and Dr. Surajeet Ghosh and Mr. George Reins for providing the experimental data for the plunging wave breaking simulations.

References

Aulisa, E., Manservisi, S., Scardovelli, R., Zaleski, S., 2007. Interface reconstruction with least-squares fit and split advection in three-dimensional Cartesian geometry. J. Comput. Phys. 225, 2301–2319.

Balay, S., Gropp, W., McInnes, L., Smith, B., 1997. Efficient management of parallelism in object-oriented numerical software libraries. In: Arge, E., Bruaset, A., Langtangen, H. (Eds.), Modern Software Tools in Scientific Computing. Birkhauser Press, Cambridge, MA, pp. 163–202.

Bhaga, D., Weber, M.E., 1981. Bubbles in viscous liquids: shape, wakes and velocities. J. Fluid Mech. 105, 61–85.

Bonmarin, P., 1989. Geometric properties of deep-water breaking waves. J. Fluid Mech. 209, 405–433.

Bourlioux, A., 1995. A coupled level-set volume-of-fluid algorithm for tracking material interfaces. In: Proceedings of Sixth International Symposium on Computational Fluid Dynamics, Lake Tahoe, CA, USA.

Carrica, P.M., Wilson, R.V., Stern, F., 2007. An unsteady single-phase level set method for viscous free surface flows. Int. J. Numer. Methods Fluids 53, 229–256.

Chang, K.-A., Liu, P.L.-F., 1999. Experimental investigation of turbulence generated by breaking waves in water of intermediate depth. Phys. Fluids 11, 3390–3400.

Chen, G., Kharif, C., Zaleski, S., Li, J., 1999. Two-dimensional Navier–Stokes simulation of breaking waves. Phys. Fluids 11, 121–133.

Dommermuth, D.G., Sussman, M., Beck, R.F., O'Shea, T.T., Wyatt, D.C., Olson, K., MacNeice, P., 2004. The numerical simulation of ship waves using cartesian grid methods with adaptive mesh refinement. In: Proceedings of the 25th ONR Symposium on Naval Hydrodynamics, St. John's Newfoundland and Labrador, Canada.

Enright, D., Fedkiw, R., Ferziger, J., Mitchell, I., 2002. A hybrid particle level set method for improved interface capturing. J. Comput. Phys. 183, 83–116.

Ghosh, S., Reins, G., Koo, B., Wang, Z., Yang, J., Stern, F., 2007. Plunging wave breaking: EFD and CFD. In: International Conference on Violent Flows 2007, Fukuoka, Japan.

Ghosh, S., 2008. Free surface instabilities and plunging breaking waves downstream of a bump in a shallow water open channel flume. Ph.D. Thesis, The University of Iowa, USA.

Gueyffier, D., Li, J., Nadim, A., Scardovelli, S., Zaleski, S., 1999. Volume of fluid interface tracking with smoothed surface stress methods for three-dimensional flows. J. Comput. Phys. 152, 423–456.

Hirt, C., Nichols, B., 1981. Volume of fluid (VOF) method for the dynamics of free boundaries. J. Comput. Phys. 39, 201–225.

Hua, J., Stene, J.F., Lin, P., 2008. Numerical simulation of 3D bubbles rising in viscous liquids using a front tracking method. J. Comput. Phys. 227, 3358–3382.

Iafrati, A., Mascio, D., Campana, E.F., 2001. A level set technique applied to unsteady free surface flows. Int. J. Numer. Methods Fluids 35, 281–297.

Jiang, G., Peng, D., 1999. Weighted ENO schemes for Hamilton–Jacobi equations. SIAM J. Sci. Comput. 21, 2126–2143.

Klemt, M., 2005. RANSE simulation of ship seakeeping using overlapping grids. Ship Technol. Res. 52, 65–81.

Leonard, B.P., 1979. A stable and accurate convective modeling procedure based on quadratic upstream interpolation. Comput. Methods Appl. Mech. Eng. 19, 59–98.

Lopez, J., Hernandez, J., Gomez, P., Faura, F., 2005. An improved PLIC-VOF method for tracking thin fluid structures in incompressible two-phase flows. J. Comput. Phys. 208, 51–74.

Lubin, P., Vincent, S., Abadie, S., Caltagirone, J.-P., 2006. Three-dimensional large eddy simulation of air entrainment under plunging breaking waves. Coastal Eng. 53, 631–655.

Melville, W.K., Veron, F., White, C.J., 2002. The velocity field under breaking waves: coherent structures and turbulence. J. Fluid Mech. 454, 203–233.

Menard, T., Tanguy, S., Berlemont, A., 2007. Coupling level set/VOF/ghost fluid methods: validation and application to 3D simulation of the primary break-up of a liquid jet. Int. J. Multiphase Flow 33, 510–524.

Morton, D., Rudman, M., Liow, J.-L., 2000. An investigation of the flow regimes resulting from splashing drops. Phys. Fluids 12, 747–763.

Osher, S., Sethian, J.A., 1988. Fronts propagating with curvature-dependent speed: algorithms based on Hamilton–Jacobi formulations. J. Comput. Phys. 79, 12–49.

Peng, D.P., Merriman, B., Osher, S., Zhao, H., Kang, M., 1999. A PDE-based fast local level set method. J. Comput. Phys. 155, 410–438.

Peregrine, D.H., 1983. Breaking waves on beaches. Ann. Rev. Fluid Mech. 15, 149–178.

Reins, G., 2008. Experimental study of an impulsive plunging breaker downstream of a bump in a shallow water open channel flume. Master's Thesis, The University of Iowa, USA.

Scardovelli, R., Zaleski, S., 2000. Analytical relations connecting linear interfaces and volume fractions in rectangular grids. J. Comput. Phys. 164, 228–237.

Scardovelli, R., Zaleski, S., 2003. Interface reconstruction with least-square fit and split Eulerian–Lagrangian advection. Int. J. Numer. Methods Fluids 41, 251–274.

Shu, C.W., Osher, S., 1988. Efficient implementation of essentially non-oscillatory shock-capturing schemes. J. Comput. Phys. 77, 439–471.

Son, G., Hur, N., 2002. A coupled level set and volume-of-fluid method for the buoyancy-driven motion of fluid particles. Numer. Heat Transfer B 42, 523–542.

Son, G., 2003. Efficient implementation of a coupled level-set and volume-of-fluid method for three-dimensional incompressible two-phase flows. Numer. Heat Transfer B 43, 549–565.

Strain, J., 1999. Tree methods for moving interfaces. J. Comput. Phys. 151, 616–648.

Sussman, M., Almgren, A., Bell, J., Colella, P., Howell, L., Welcome, M., 1999. An adaptive level set approach for incompressible two-phase flows. J. Comput. Phys. 148, 81–124.

Sussman, M., Puckett, E.G., 2000. A coupled level set and volume-of-fluid method for computing 3D axisymmetric incompressible two-phase flows. J. Comput. Phys. 162, 301–337.

Sussman, M., Smereka, P., Osher, S., 1994. A level set approach for computing solutions to incompressible two-phase flow. J. Comput. Phys. 114, 146–159.

Tallent, J.R., Yamashita, T., Tsuchiya, Y., 1990. Transformation characteristics of breaking waves. Wave Water Kinematics 178, 509–523.

Toomas LIIV., 2001. Investigation of turbulence in a plunging breaking wave. In: Proceedings Estonian Acad. Sci. Eng., vol. 7, pp. 58–78.

Unverdi, S.O., Tryggvason, G., 1992. A front-tracking method for viscous, incompressible, multi-fluid flows. J. Comput. Phys. 100, 25–37.

Watanabe, Y., Saeki, H., Hosking, R.J., 2005. Three-dimensional vortex structures under breaking waves. J. Fluid Mech. 545, 291–328.

Yang, J., Balaras, E., 2006. An embedded-boundary formulation for large-eddy simulation of turbulent flows interacting with moving boundaries. J. Comput. Phys. 215, 12–40.

Yang, J., Stern, F., 2007a. A sharp interface method for two-phase flows interacting with moving bodies. In: 18th AIAA Computational Fluid Dynamics Conference, Miami, FL, USA, AIAA Paper 2007-4578.

Yang, J., Stern, F., 2007b. Large-eddy simulation of breaking waves using embedded-boundary/level-set method. In: 45th AIAA Aerospace Sciences Meeting and Exhibit, Reno, Nevada, USA, AIAA Paper 2007-1455.

Yang, X., James, A.J., Lowengrub, J., Zheng, X., Cristini, V., 2007. An adaptive coupled level-set/volume-of-fluid interface capturing method for unstructured triangular grids. J. Comput. Phys. 217, 364–394.